2D Materials

LETTER

Thermal transport across graphene step junctions

Miguel Muñoz Rojo[1,2,9], **Zuanyi Li**[1,9], **Charles Sievers**[3], **Alex C Bornstein**[1], **Eilam Yalon**[1], **Sanchit Deshmukh**[1], **Sam Vaziri**[1], **Myung-Ho Bae**[4], **Feng Xiong**[5], **Davide Donadio**[3,8] and **Eric Pop**[1,6,7,8]

1 Department of Electrical Engineering, Stanford University, Stanford, CA 94305, United States of America
2 Department of Thermal and Fluid Engineering, University of Twente, Enschede, 7500 AE, Netherlands
3 Department of Chemistry, University of California Davis, Davis, CA 95616, United States of America
4 Korea Research Institute of Standards and Science, Daejeon 34113, Republic of Korea
5 Department of Electrical and Computer Engineering, University of Pittsburgh, Pittsburgh, PA 15261, United States of America
6 Department of Materials Science and Engineering, Stanford University, Stanford, CA 94305, United States of America
7 Precourt Institute for Energy, Stanford University, Stanford, CA 94305, United States of America
8 Author to whom any correspondence should be addressed.
9 These authors contributed to this work equally.

E-mail: epop@stanford.edu and ddonadio@ucdavis.edu

Keywords: graphene junction, thermal conductance, molecular dynamics, thermal rectification

Supplementary material for this article is available online

Abstract

Step junctions are often present in layered materials, i.e. where single-layer regions meet multilayer regions, yet their effect on thermal transport is not understood to date. Here, we measure heat flow across graphene junctions (GJs) from monolayer-to-bilayer graphene, as well as bilayer to four-layer graphene for the first time, in both heat flow directions. The thermal conductance of the monolayer-bilayer GJ ranges from ~0.5 to 9.1 $\times$ 10^8 W m^{-2} K^{-1} between 50 K to 300 K. Atomistic simulations of such a GJ device reveal that graphene layers are relatively decoupled, and the low thermal conductance of the device is determined by the resistance between the two distinct graphene layers. In these conditions the junction plays a negligible effect. To prove that the decoupling between layers controls thermal transport in the junction, the heat flow in both directions was measured, showing no evidence of thermal asymmetry or rectification, within experimental error bars. For large-area graphene applications, this signifies that small bilayer (or multilayer) islands have little or no contribution to overall thermal transport.

1. Introduction

The emergence of two-dimensional (2D) materials has brought new opportunities to explore fundamental physical properties and to exploit these materials for new applications [1]. As the first isolated 2D material [2–4] and due to its extraordinary transport properties [5], graphene has been extensively studied especially for electronic applications. However, the properties of graphene can be altered due to crystal imperfections which appear, for example, during graphene growth by chemical vapor deposition (CVD). One such type are grain boundaries (GBs) [6], i.e. line defects where two graphene grains (of the same thickness) are stitched together. Other defects are graphene junctions (GJs), i.e. the steps between regions with different number of graphene layers, such as monolayer-to-bilayer (1L–2L) junctions.

The properties of GBs are relatively well understood, having been measured electrically [7], thermally [8], and mechanically [9]. For example, GBs reduce the overall electrical [7] and thermal conductivity [10, 11] of graphene due to electron and phonon scattering, respectively. However, GJs have only recently attracted more interest with few experimental studies of their properties in electronics [12], optoelectronics [13], and as p-n junctions [14]. A theoretical study assigned thermal rectification properties to GJs [15], however this has not been examined experimentally. Other simulations also showed that heat transfer at GJs is non-trivial, because in the multilayer region different layers may have different temperatures [16]. Knowledge of heat flow across GJs is important not just fundamentally, but also for practical applications in terms of how they modify the overall thermal conductivity of graphene (as GBs do [10, 17]), or where GJs could act as

phonon filters. As an example, electronic devices based on graphene and other 2D materials often contain GJs, but little is known about how their thermal resistance affects the overall device performance [18, 19].

Here, we investigate for the first time the temperature-dependent heat flow across GJs supported on SiO$_2$ substrates. Our experimental results combined with molecular and lattice dynamics (MD and LD) simulations indicate thermal decoupling between layers caused by a large thermal boundary resistance (TBR). Thus, we establish a microscopic understanding of thermal conduction across GJs and clarify their role in large-area thermal management applications of graphene.

2. Experimental results

Figure 1(a) illustrates the schematic of the device structure we used to measure the thermal conductance across GJs. Graphene used in this study (see Methods) is mechanically exfoliated onto a SiO$_2$/Si substrate (supplementary section 1 (stacks.iop.org/TDM/6/011005/mmedia)) and step junctions were identified by optical microscopy, atomic force microscopy (AFM), Raman spectroscopy (see Methods) and were finally confirmed by scanning electron microscopy (SEM) after all measurements were completed. During thermal measurements two parallel metal lines were used as the heater and thermometer, interchangeably [20, 21]. A thin layer of SiO$_2$ (~40 nm, electron-beam evaporated, see Methods) underneath the metal lines provided electrical isolation from the graphene. Figures 1(b) and (d) show SEM images of the two devices measured, which correspond to 1L–2L and 2L–4L (bilayer to four-layer) GJs, respectively. Figures 1(c) and (e) show Raman spectra obtained on each side of the GJ, determining the number of graphene layers. The Raman spectra do not show discernible D peaks even after patterning the metal lines, confirming relatively defect-free, crystalline graphene regions (supplementary section 2).

We performed heat flow measurements from 50 K to 300 K on these GJ samples and on similar control samples without graphene. We also measured heat flow across the GJs in both directions by swapping the heater and sensor, to test for possible asymmetry in the heat flow as a consequence of phonon scattering at the junction, which would lead to thermal rectification for large temperature differentials [15]. The measurements are performed as follows. Current is forced into a metal line, which acts as a heater, while both metal lines are used to sense temperature, setting up a temperature gradient across the GJ. The metal lines are thermo-resistive elements, which allow us to convert measured changes of electrical resistance into variation of the temperature of the sensor, ΔT_S, and heater, ΔT_H, as a function of the heater power P_H (supplementary section 4). We calibrated both metal lines for each sample by monitoring the resistance over a slightly wider temperature range, from 40 K to 310 K,

to determine the temperature coefficient of resistance (TCR) and quantify temperature variations (supplementary sections 6 and 7).
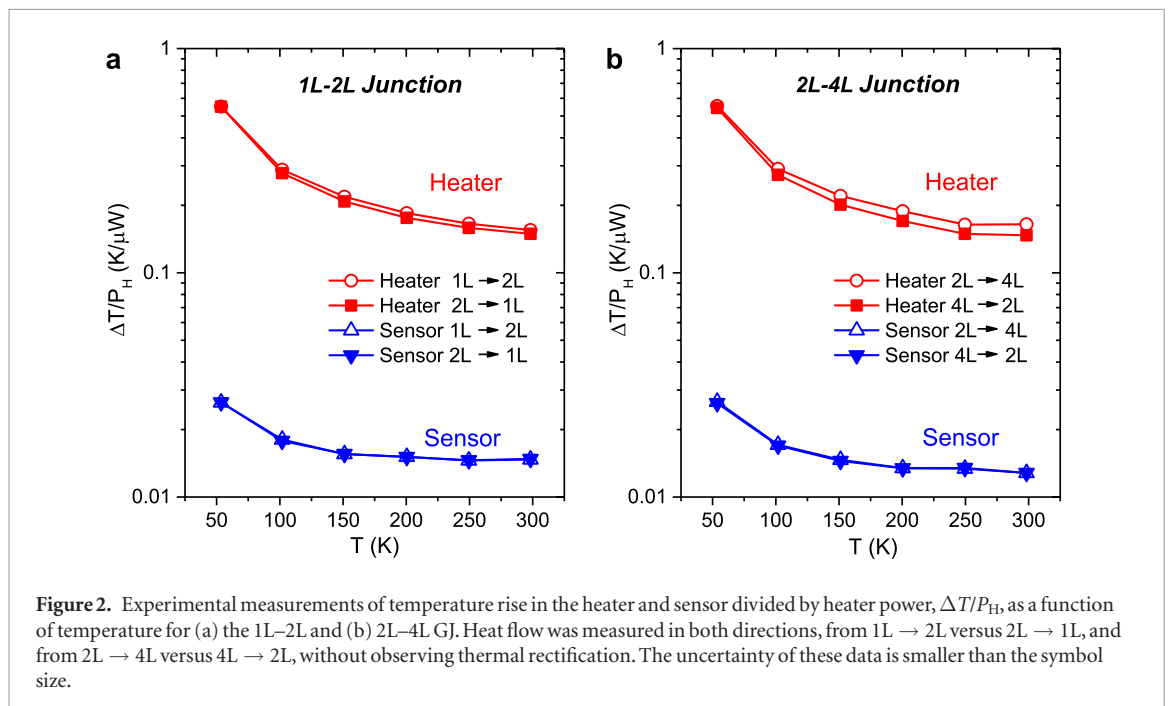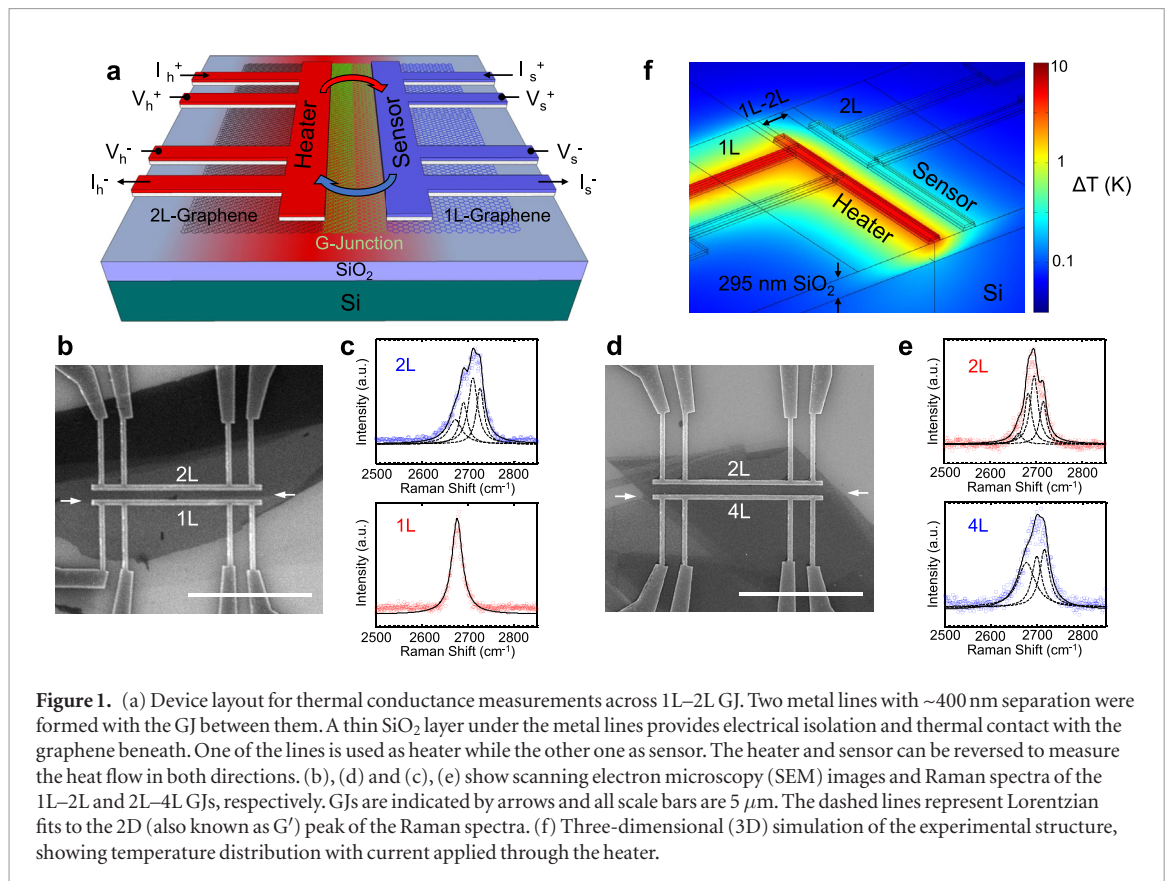
Once the temperature difference between the metal lines is known as a function of heater power, the thermal conductance across the junction is obtained by processing the experimental data using a three-dimensional (3D) finite element model (FEM) [20, 22] (see Methods). In this simulation, the graphene channel region between heater and sensor is treated with an effective thickness $h = 0.34n$ nm, where $n = 2$ in both devices because most of the two channels are covered by 2L graphene (see arrows in figures 1(b) and (d)). In other words, the FEM fits the graphene channel with an effective thermal conductivity, k, between heater and sensor. The effective channel thermal conductance is $G = kh(W/L)$, where W and L are the graphene channel width and length.

The FEM shown in figure 1(f) accurately replicates the experimental setup taking into account: (i) all geometric dimensions of the metal lines, determined using SEM images (supplementary section 1); (ii) the thickness of the SiO$_2$ under the graphene from ellipsometry (supplementary section 3) and its temperature-dependent thermal conductivity from measurements of the control sample (supplementary section 5); (iii) the Si thermal conductivity for Si wafers with the same doping density [23] (supplementary section 3). The FEM also includes the effect of TBR at Si–SiO$_2$ interfaces [20] from the control sample, graphene–SiO$_2$ [24] and SiO$_2$-metal [25] interfaces, based on previous measurements of similar samples [20]. Figure 1(f) shows the simulated temperature distribution with current applied through the heater for the 1L–2L junction device. The thermal conductivity k of the graphene channel is varied in the simulation until ΔT_S and ΔT_H versus P_H modeling results match well with the experimental data.

We also measured a control sample without graphene in the channel to validate our method and to obtain the thermal properties of the parallel heat flow path through the contacts, the supporting SiO$_2$, the SiO$_2$–Si interface and the Si substrate (supplementary section 5). These thermal properties obtained after processing the experimental data with the FEM show good agreement with well-known data from literature [20, 26, 27] over the full temperature range. Consequently, these data were used as inputs for the FEM simulation of the GJ structures.

Figure 2 shows the experimental heater temperature rise (in red) and sensor temperature rise (in blue) normalized by the heater power, $\Delta T/P_H$, as a function of temperature obtained for the two junctions studied, 1L–2L and 2L–4L. The heat flow was studied in both directions across the GJ to account for possible thermal rectification effects. The uncertainty of $\Delta T/P_H$ is ~0.5%–1%, which agrees well with our previous experiments that used similar metal lines [20].
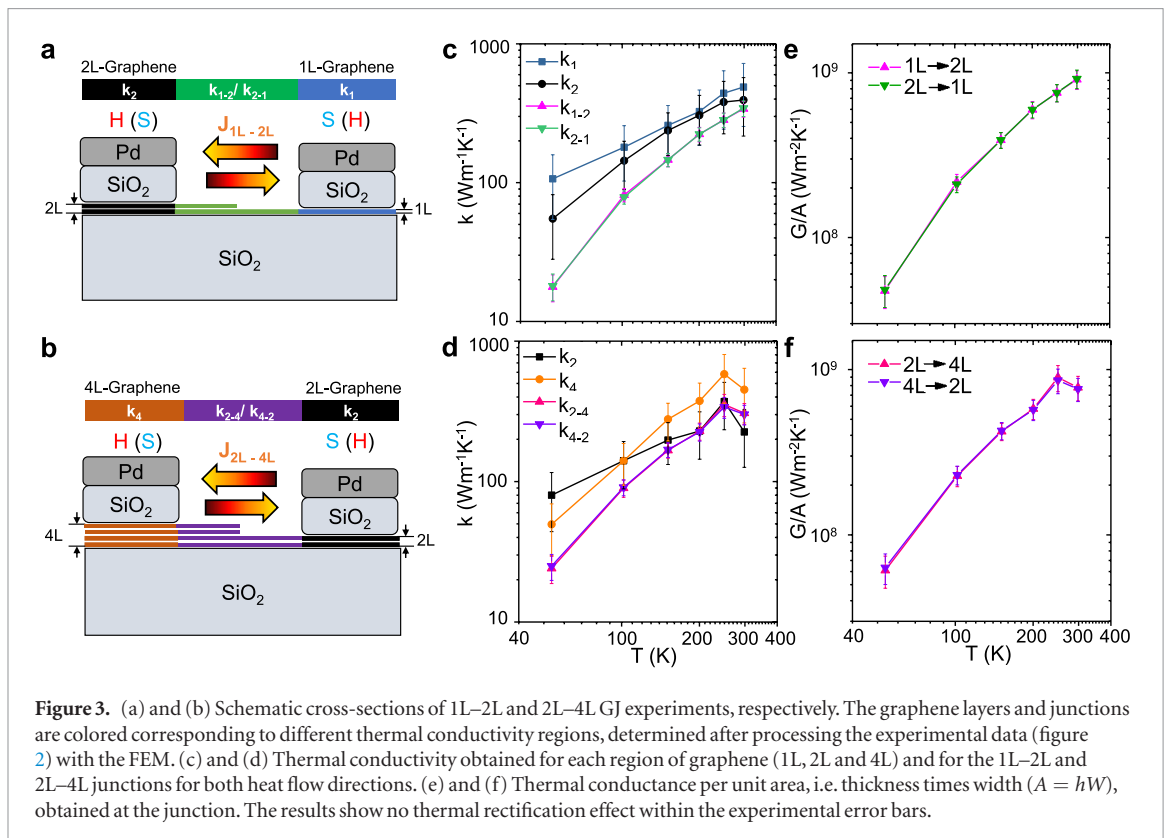
Figures 3(a) and (b) show the schematic of the 1L–2L and 2L–4L GJ samples. The rectangular colored sec-

Figure 1. (a) Device layout for thermal conductance measurements across 1L–2L GJ. Two metal lines with ~400 nm separation were formed with the GJ between them. A thin SiO_2 layer under the metal lines provides electrical isolation and thermal contact with the graphene beneath. One of the lines is used as heater while the other one as sensor. The heater and sensor can be reversed to measure the heat flow in both directions. (b), (d) and (c), (e) show scanning electron microscopy (SEM) images and Raman spectra of the 1L–2L and 2L–4L GJs, respectively. GJs are indicated by arrows and all scale bars are 5 μm. The dashed lines represent Lorentzian fits to the 2D (also known as G') peak of the Raman spectra. (f) Three-dimensional (3D) simulation of the experimental structure, showing temperature distribution with current applied through the heater.

Figure 2. Experimental measurements of temperature rise in the heater and sensor divided by heater power, $\Delta T/P_{\mathrm{H}}$, as a function of temperature for (a) the 1L–2L and (b) 2L–4L GJ. Heat flow was measured in both directions, from 1L $\rightarrow$ 2L versus 2L $\rightarrow$ 1L, and from 2L $\rightarrow$ 4L versus 4L $\rightarrow$ 2L, without observing thermal rectification. The uncertainty of these data is smaller than the symbol size.

tions on top illustrate the thermal conductivities, i.e. 1L (k_1), 2L (k_2) and 4L (k_4) for non-junction regions, while 1L–2L (k_{1-2}) and 2L–4L (k_{2-4}) represent the GJ channel region. These are used by the FEM to process the raw experimental data from figure 2, yielding the effective thermal conductivities shown in figures 3(c)–(f). While the effective thermal conductivity of the GJ channel (k_{1-2} and k_{2-4}) is determined from the temperature gradient between heater and sensor, the thermal conductivity of 1L, 2L and 4L is mainly determined

from temperature variations only at the heater surroundings. Although not the main topic of this study, these supported 2L and 4L graphene thermal conductivity estimates are among the first of their kind (others being discussed below).

Figures 3(c) and (d) display the extracted thermal conductivity of the 1L, 2L and 4L graphene regions, as well as the effective thermal conductivity of the 1L–2L and 2L–4L junctions, in both directions of heat flow. The 1L, 2L and 4L thermal conductivities show simi-
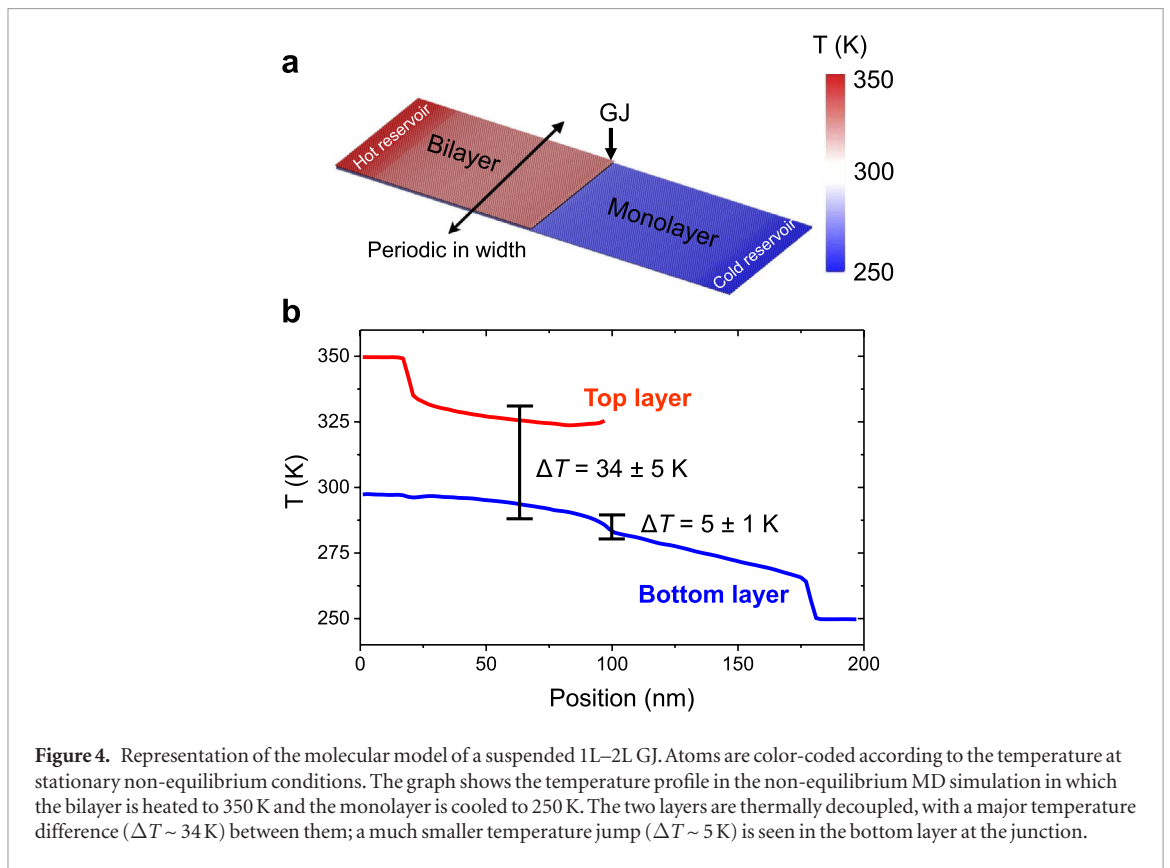
Figure 3. (a) and (b) Schematic cross-sections of 1L–2L and 2L–4L GJ experiments, respectively. The graphene layers and junctions are colored corresponding to different thermal conductivity regions, determined after processing the experimental data (figure 2) with the FEM. (c) and (d) Thermal conductivity obtained for each region of graphene (1L, 2L and 4L) and for the 1L–2L and 2L–4L junctions for both heat flow directions. (e) and (f) Thermal conductance per unit area, i.e. thickness times width ($A = hW$), obtained at the junction. The results show no thermal rectification effect within the experimental error bars.

lar values over the entire range of temperature. Their room temperature values are ~500 Wm^{-1} K^{-1} for 1L, ~400 Wm^{-1} K^{-1} for 2L, and ~450 Wm^{-1} K^{-1} for 4L graphene, respectively. These are consistent with earlier measurements by Seol *et al* [28], Sadeghi *et al* [29], and by Jang *et al* [21] who found the thermal conductivity of SiO$_2$-supported 1L, 2L and 4L graphene were ~580, ~600 and ~480 Wm^{-1} K^{-1} at room temperature, respectively. To obtain the various thermal conductivities from the FEM fitting, we used the same TBR between graphene and SiO$_2$ for all layers, following Chen *et al* [24], but there may be small differences in the TBR that could be behind this small variation. However, our results are in good agreement with values reported by Sadeghi *et al* [29], which show that the thermal conductivity of SiO$_2$-supported graphene few-layers remains very similar.

In comparison, figures 3(c) and (d) show that the effective thermal conductivity in the GJ regions, i.e. k_{1-2} and k_{2-4}, is lower than in the graphene layers, i.e. k_1, k_2 and k_4. This difference becomes more evident as the temperature reduces from 300 K to 50 K. Figures 3(e) and (f) show the effective thermal conductance of the GJ regions, calculated by dividing the thermal conductivity with the metal line separation (see Methods). The thermal conductance for 1L–2L varies from $4.8 \pm 1.1 \times 10^7$ W m^{-2} K^{-1} to $9.1 \pm 1.2 \times 10^8$ W m^{-2} K^{-1} at 50 K and 300 K respectively, while for 2L–4L it varies from $6.1 \pm 1.3 \times 10^7$ W m^{-2} K^{-1} to $7.7 \pm 1.2 \times 10^8$ W m^{-2} K^{-1} at 50 K and 300 K respectively. Bae *et al* [20] explained that as we shorten the length of a graphene channel, quasi-ballistic phonon transport effects reduce its thermal conductivity,

because the longest phonon mean free paths become limited by the length of the channel. In other words, the graphene thermal conductivity is length-dependent in this sub-micron regime. The thermal conductivity of our GJ samples is consistent with values reported by Bae *et al* [20] for length-dependent graphene without junctions. Additionally, that the thermal conductance of the 1L–2L and 2L–4L channels is almost identical for both heat flow directions, i.e. $k_{1-2} \approx k_{2-1}$ and $k_{2-4} \approx k_{4-2}$, indicates no measurable asymmetry in the heat flow or thermal rectification effects on supported graphene at the junction.

3. Molecular and Lattice dynamic simulations and discussion

To explain the measured thermal conductance of the GJs in both heat flow directions we consider two possible scenarios. The first scenario consists of thermal decoupling between the top and bottom layers of graphene, which could be attributed to the presence of a large TBR between layers. The thermal decoupling between layers would cause the heat to flow only through one layer, i.e. the bottom one, which would result in similar conductance values as the work of Bae *et al* [20]. Moreover, the large TBR between layers would make phonon scattering at the junction negligible, which would support the idea of a non-asymmetry or thermal rectification effect. The second possible scenario would be a perfect coupling between the top and bottom graphene layers, i.e. very small TBR between layers, which would explain the similarity of the GJs thermal conductance with

Figure 4. Representation of the molecular model of a suspended 1L–2L GJ. Atoms are color-coded according to the temperature at stationary non-equilibrium conditions. The graph shows the temperature profile in the non-equilibrium MD simulation in which the bilayer is heated to 350 K and the monolayer is cooled to 250 K. The two layers are thermally decoupled, with a major temperature difference ($\Delta T \sim 34\,$K) between them; a much smaller temperature jump ($\Delta T \sim 5\,$K) is seen in the bottom layer at the junction.

those shown by Bae *et al* [20]. However, under these circumstances, we would expect the junction to scatter phonons more efficiently, which might induce some thermal asymmetry across the junction.

To quantitatively understand the phonon physics at the GJ, we performed atomistic molecular dynamics (MD) simulations and LD calculations (see Methods). First, we evaluate a *suspended* 1L–2L junction by non-equilibrium molecular dynamics (NEMD) simulations [30] as shown in figure 4. The length of the MD models is up to 200 nm, which, although about half the size of the experimental device, still captures its essential physical properties. To produce a stationary heat current (J), the ends of the device are kept at 350 and 250 K (see Methods), respectively, by two Langevin thermostats. If the system displayed thermal rectification its thermal conductance, computed as $G = J/\Delta T$, would differ if the heat current went from 1L → 2L or from 2L → 1L. Setting up the NEMD simulations we have two options to treat the bilayer side of the GJ: we can either apply the thermostat to both layers, as in [16], or treat only the top layer as a thermal bath. In the first case we find that the thermal conductance is near that of a single graphene layer, too large compared to the experiments (supplementary section 8). Thus, we focus our analysis on the second case. In fact, NEMD simulations show the thermal conductance of the device is the same, within the statistical uncertainty, regardless of the direction of the heat current. Hence, our simulations also confirm that this system does not display thermal rectification.

An analysis of the temperature profile at stationary conditions (figure 4) shows that the top and bottom layers of the junction are thermally decoupled, and the main source of TBR is not the step at the junction, but rather the weak coupling between the two stacked graphene layers. Such weak coupling causes a larger temperature difference ($\Delta T \sim 34\,$K) between the top and bottom layer of the device, whereas the temperature discontinuity at the step of the junction is only ~5 K. Hence the main resistive process occurs at the interface between the overlapping layers, which is symmetric, thus explaining why no thermal asymmetry or rectification occurs. Even with a very large temperature difference at the two ends of the device ($\Delta T \sim 450\,$K), thermal rectification remains negligible (supplementary section 8).

Our experiments and simulations appear at odds with the NEMD results of Zhong *et al* [15]. In this work, the system is set up such that there is no thermal decoupling between layers in the thermal reservoir, and this effect is not probed in the non-thermostated junction. Hence these former simulations suggest an asymmetric phonon scattering at the junction that depends on the heat flow direction (thermal rectification effect). By comparing our simulations with theirs, we conclude that an apparent thermal rectification could be observed by sampling the system at non-stationary conditions, stemming from poor equilibration of the thermal baths. This is especially a problem for poorly ergodic systems such as graphene and carbon nanotubes [31].

While NEMD sheds light on the microscopic details of heat transport at the GJ, it does not allow a quantitative estimate of the conductance that can be compared to experiments. In fact, due to the classical nature of MD simulations, quantum effects are not taken into account. Considering that the Debye temperature of graphene exceeds 2000 K and experiments are carried out at room temperature and below, quantum effects are expected to play a major role in determining the conductance. Thus, we also calculated the thermal conductance of the 1L–2L junction, treated as an open system, using the elastic scattering kernel method (ESKM) [32]. ESKM is an LD approach equivalent to Green's functions [33], implemented in a scalable code that allows us to compute coherent phonon transport in systems of up to 10^6 atoms [34]. Thus, we could calculate the thermal conductance of suspended and SiO_2-supported GJs with the same overlap length as in the experiments. LD calculations give the phonon transmission function $\mathcal{T}(\omega)$ for an open system with semi-infinite thermal reservoirs, resolved by mode frequency and polarization. The thermal conductance is then computed by the Landauer formula [35], integrating $\mathcal{T}(\omega)$ over all frequencies:

$$G = \frac{1}{2\pi} \int_0^{\omega_{max}} d\omega \; \hbar\omega \mathcal{T}(\omega) \frac{\partial f_{BE}(\omega, T)}{\partial T}, \quad (1)$$

where T is the temperature and f_{BE} is the Bose–Einstein distribution function, accounting for the quantum population of phonons. In this approach we neglect anharmonic phonon-phonon scattering. This assumption is justified *a posteriori* by comparing the conductance of a suspended device with overlap length of 25 nm, computed by NEMD, $G = 1.16 \pm 0.09 \times 10^9$ W m^{-2} K^{-1}, with that obtained by LD using a classical phonon distribution function, $G = 0.92 \times 10^9$ W m^{-2} K^{-1}. A ~20% difference between LD and NEMD calculations of G is acceptable, as it may stem not only from neglecting anharmonic scattering in LD, but also from the finite ΔT in NEMD.

Figure 5 displays the thermal conductance of the 1L–2L GJ calculated by LD as a function of the length of the bilayer part (a) and of the temperature (b), compared to experimental data. To assess the effect of the substrate in the experimental device, we consider models of GJ both suspended and supported on a SiO_2 substrate. The geometry of the suspended model is the same as the one used in NEMD (figure 4). G is independent of the length of the monolayer part of the device, as in this approach it conducts heat ballistically. G is normalized by the width of the GJ and by a nominal thickness of the bilayer part of 0.67 nm, which is the same convention used in processing the experimental data.

The agreement between modeling and experiments is excellent at low temperature in figure 5. In the experimental device at higher temperature, heat transfer is still mainly dictated by the TBR between the two graphene layers, but the thermal bath also affects the bottom layer in the bilayer part of the device, thus making the conductance larger than that predicted by the model. The thermal conductance of the device increases with the interlayer overlapping surface area, which is determined by the length of the bilayer part (figure 5(a)). However, G does not grow linearly with the overlap surface and tends to saturate with the overlapping length. The conductance limit of this device is indeed dictated by the ballistic limit of a single graphene sheet [36].

The interaction with the SiO_2 substrate reduces the overall conductance of the device by about 30% at room temperature. In order to achieve quantitative agreement between theory and experiments, it is important to consider the conductance reduction in the model for supported structures. The temperature dependence of the GJ thermal conductance can be almost entirely ascribed to the quantum population of the phonon modes. In fact, figure 5(b) shows that theory and experiments display an excellent agreement at low temperature, while systematic deviations appear at $T > 200$ K, allowing us to pinpoint the effect of anharmonic scattering, which is not taken into account in the calculations. Resolving the transmission function by mode polarization shows that only out-of-plane modes contribute to heat transport across the interlayer junction, consistent with another recent study [37] (supplementary section 9). We also observe that the interaction with the substrate causes an offset of the out-of-plane modes of the bottom graphene layer with respect to those of the top layer, thus hampering the transmission function even further and reducing the conductance of the device.

4. Conclusions

In conclusion, we have experimentally measured, for the first time, the temperature-dependent heat flow across GJs, i.e. 1L–2L and 2L–4L GJs, supported on SiO_2 substrates. MD and LD simulations were used to analyze the GJ thermal transport. The simulations show that the top and bottom layers of the junction are only weakly thermally coupled, and the main source of TBR is not the step at the junction, but rather the weak coupling between the two layers in bilayer graphene. The interaction with the substrate was observed to have a significant effect to achieve good agreement between the theory and experiments. In fact, the values obtained for the experimental and theoretical thermal conductance of supported GJs showed excellent agreement at low temperature ($T < 200$ K), whose dependence can be almost entirely ascribed to the quantum population of the phonon modes. The deviations observed above 200 K, allowed us to quantify the effect of anharmonic scattering. Additionally, the thermal decoupling observed between layers suppresses the possibility of thermal rectification in GJs. Our findings shed new light on thermal transport across GJs, revealing thermal
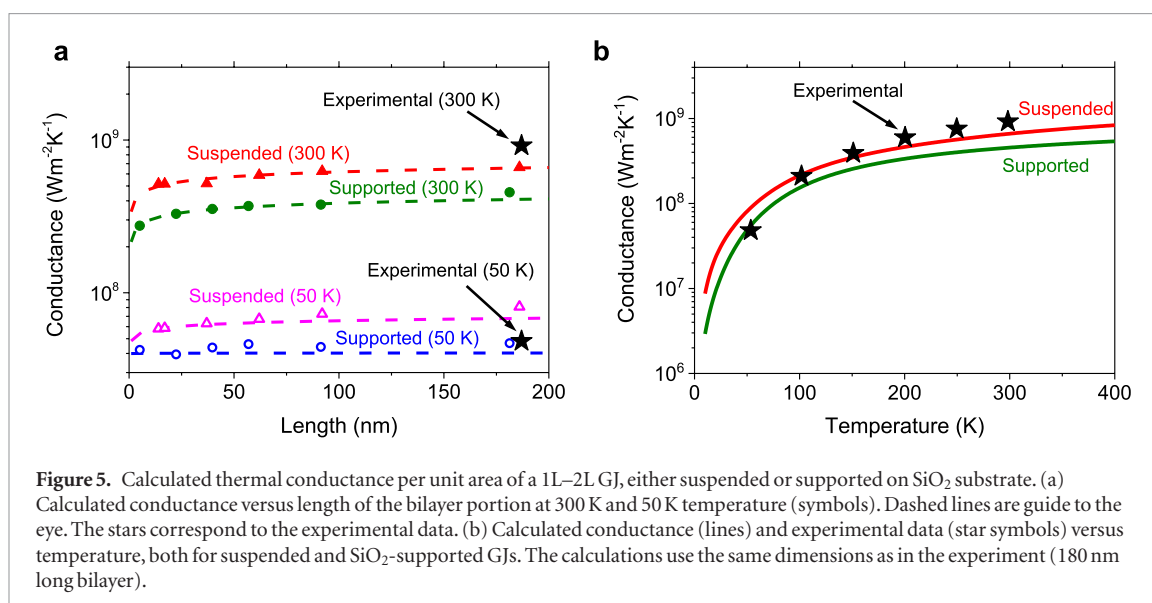
Figure 5. Calculated thermal conductance per unit area of a 1L–2L GJ, either suspended or supported on SiO_2 substrate. (a) Calculated conductance versus length of the bilayer portion at 300 K and 50 K temperature (symbols). Dashed lines are guide to the eye. The stars correspond to the experimental data. (b) Calculated conductance (lines) and experimental data (star symbols) versus temperature, both for suspended and SiO_2-supported GJs. The calculations use the same dimensions as in the experiment (180 nm long bilayer).

decoupling between layers that is behind the large TBR observed. These results also imply that the presence of GJs in large-area (e.g. CVD-grown) graphene should *not* affect the overall thermal conductivity of the material, unlike GB defects. Thus, the thermal properties of CVD-grown graphene are not expected to be affected by the presence of small bilayer islands, because most heat will be carried in the bottom layer.

4.1. Methods

4.1.1. Experimental measurements and data analysis
Highly crystalline graphite (carbon > 99.75%) was mechanically exfoliated with Scotch™ tape onto SiO_2 (~295 nm) on Si substrate chips of ~1 × 1 cm² size. An optical microscope was first used to find large GJ samples where we could perform thermal measurements (supplementary section 1).

Electron-beam (e-beam) lithography (with a first layer of PMMA 495 and a second layer of PMMA 950 spin-coated on the samples at 4000 rpm for 40 s, and baked at 180 °C for 10 min) was used to pattern the heater and sensor on each side of the GJ. Heater and sensor lines are ~200 nm wide and ~5 μm long. After development, an e-beam evaporator was used to deposit 40 nm of SiO_2 followed by 3 nm Ti and 35 nm Pd, forming the heater and sensor lines, electrically isolated from the graphene underneath (supplementary section 1). The separation (L) between heater and sensor lines for 1L–2L and 2L–4L junction samples were $L_{1L–2L} = 374$ nm and $L_{2L–4L} = 395$ nm, respectively (figures 1(b) and (d)).

Raman spectroscopy was carried out using a Horiba LabRam instrument with a 532 nm laser and 100 × objective with N.A. = 0.9, after all fabrication and other measurements were completed. The GJ region was scanned with 150 nm step size and 160 μW laser power. The laser spot diameter obtained by the knife-edge method was <400 nm. We analyzed

the spectra of several representative locations on both sides of the GJs by removing the baseline and fitting the 2D (also known as G') peak with different Lorentzians (figures 1(c) and (e)). These Raman maps determined the quality of the graphene and number of layers on each side of the GJ (also see supplementary section 2).

The samples were wire-bonded into chip carriers and the thermal measurements were carried out in a cryostat at 1.3×10^{-6} mbar, at temperatures from 50 K to 300 K (supplementary sections 4–7). SEM was used after thermal measurements to examine the location of the heater and sensor on each side of the GJ, as well as to measure the separation and dimensions of the lines (supplementary section 1).

The experimental data were analyzed using finite element modeling (FEM) with COMSOL® Multiphysics (supplementary section 10), to determine the thermal conductance of the GJ and of the various layers and interfaces. These simulations were based on previous measurements on similar samples carried out by a subset of the authors [20, 22]. The uncertainty calculations are also explained in supplementary section 10.

4.1.2. Non-equilibrium molecular dynamics (NEMD)
All MD simulations were carried using the LAMMPS package [38]. We used the optimized Tersoff force-field [39] for the in-plane interactions, and a Lennard–Jones (LJ) potential with $\epsilon = 3.29567$ meV and $\sigma = 3.55$ Å for the interlayer interactions, according to the OPLS-AA parameterization [40]. Equations of motion were integrated with a time step of 1 fs. The simulated structure had a periodic width of 5 nm and interlayer spacing of 0.335 nm, containing 14736 C atoms in a 25 nm long top layer (4896 atoms) and a 50 nm bottom layer (9840 atoms) in the transport direction. Boundary conditions were fixed in the transport direction and periodic in both perpendicular directions. We first equilibrated the

system in the canonical ensemble at 300 K using the stochastic velocity rescaling algorithm [41] for 0.1 ns (supplementary section 8).

To enable a stationary heat current, the 10% C atoms at the left end of the top layer and 10% atoms at the end of the bottom layer were thermostatted to the target temperatures of 350 and 250 K, respectively, using Langevin thermostats with a 0.05 ps relaxation time. We have tested different coupling constants and verified that a weaker coupling, e.g. 1 ps, is insufficient for the thermal baths to reach the target temperatures [31]. The first two rows of C atoms in the top and bottom sheets and the last two rows of C atoms in the bottom sheet were constrained at fixed positions, and the system was allowed to run for a total of 40 ns. The temperature profile was grouped into 100 bins along the transport direction, sampled every 10th step, the total average was computed every 1000 steps and the temperature was calculated from the kinetic energy. The power supplied or subtracted by the hot or cold Langevin thermal baths is averaged over time at stationary conditions to give the steady-state heat flux. The temperature profiles of the converged steady-state are averaged and plotted, and the difference in bath temperature gives the total temperature differential (supplementary section 8).

4.1.3. LD calculations

We compute thermal boundary conductance in the quantum regime for GJs models using LD and the ESKM [32]. We consider both suspended and supported junctions. The interatomic potentials used for LD calculations were the same as in the NEMD simulations for the suspended device. The interatomic interactions of the quartz substrate in the supported device are modeled with the potential by van Beest *et al* [42]. The interactions between the graphene layers and the substrate are modeled with a LJ potential with interaction cut-offs set to 8 Å. All models had a periodic width of 4.984 nm and varying lengths. The overlap lengths for the suspended GJs were 14, 17, 37, 62, 92, and 186 nm. The overlap lengths for the supported GJs were 5.1, 22.4, 39.7, 56.9, 91.4 and 181.3 nm (supplementary section 9).

Acknowledgments

Additional information

Supplementary Information is available in the online version of the paper.

Competing financial interests

The authors declare no competing financial interests.

ORCID iDs

Miguel Muñoz Rojo ● https://orcid.org/0000-0001-9237-4584
Zuanyi Li ● https://orcid.org/0000-0002-9347-5130
Sam Vaziri ● https://orcid.org/0000-0003-1234-6060
Myung-Ho Bae ● https://orcid.org/0000-0002-6884-2859
Davide Donadio ● https://orcid.org/0000-0002-2150-4182
Eric Pop ● https://orcid.org/0000-0003-0436-8534

References

[1] Houssa M, Dimoulas A and Molle A 2016 *2D Materials for Nanoelectronics* ed Taylor & Francis Group (Boca Raton, FL: CRC Press)

[2] Allen M J, Tung V C and Kaner R B 2010 Honeycomb carbon: a review of graphene *Chem. Rev.* **110** 132–45

[3] Pop E, Varshney V and Roy A K 2012 Thermal properties of graphene: fundamentals and applications *MRS Bull.* **37** 1273–81

[4] Xu Y, Li Z and Duan W 2014 Thermal and thermoelectric properties of graphene *Small* **10** 2182–99

[5] Peres N M R 2010 Colloquium: the transport properties of graphene: an introduction *Rev. Mod. Phys.* **82** 2673–700

[6] Huang P Y *et al* 2011 Grains and grain boundaries in single-layer graphene atomic patchwork quilts *Nature* **469** 389–92

[7] Tsen A W, Brown L, Levendorf M P, Ghahari F, Huang P Y, Havener R W, Ruiz-Vargas C S, Muller D A, Kim P and Park J 2012 Tailoring electrical transport across grain boundaries in polycrystalline graphene *Science* **336** 1143–6

[8] Yasaei P, Fathizadeh A, Hantehzadeh R, Majee A K, El-Ghandour A, Estrada D, Foster C, Aksamija Z, Khalili-Araghi F and Salehi-Khojin A 2015 Bimodal phonon scattering in graphene grain boundaries *Nano Lett.* **15** 4532–40

[9] Wei Y, Wu J, Yin H, Shi X, Yang R and Dresselhaus M 2012 The nature of strength enhancement and weakening by pentagon–heptagon defects in graphene *Nat. Mater.* **11** 759–63

[10] Serov A Y, Ong Z-Y and Pop E 2013 Effect of grain boundaries on thermal transport in graphene *Appl. Phys. Lett.* **102** 033104

[11] Fan Z, Hirvonen P, Pereira L, Ervasti M, Elder K, Donadio D, Harju A and Ala-Nissila T 2017 Bimodal grain-size scaling of thermal transport in polycrystalline graphene from large-scale molecular dynamics simulations *Nano Lett.* **17** 5919–24

[12] Giannazzo F, Deretzis I, La Magna A, Roccaforte F and Yakimova R 2012 Electronic transport at monolayer-bilayer junctions in epitaxial graphene on SiC *Phys. Rev.* B **86** 235422

[13] Xu X, Gabor N M, Alden J S, van der Zande A M and McEuen P L 2010 Photo-thermoelectric effect at a graphene interface junction *Nano Lett.* **10** 562–6

[14] Wang X, Xie W, Chen J and Xu J 2014 Homo- and hetero-p-n junctions formed on graphene steps *ACS Appl. Mater. Interfaces* **6** 3–8

[15] Zhong W, Huang W, Deng X and Ai B 2011 Thermal rectification in thickness-asymmetric graphene nanoribbons *Appl. Phys. Lett.* **99** 193104

[16] Rajabpour A, Fan Z and Vaez Allaei S M 2018 Inter-layer and intra-layer heat transfer in bilayer/monolayer graphene van der Waals heterostructure: is there a Kapitza resistance analogous? *Appl. Phys. Lett.* **112** 233104

[17] Ma T *et al* 2017 Tailoring the thermal and electrical transport properties of graphene films by grain size engineering *Nat. Commun.* **8** 14486

[18] Pop E 2010 Energy dissipation and transport in nanoscale devices *Nano Res.* **3** 147–69

[19] Islam S, Li Z, Dorgan V E, Bae M-H and Pop E 2013 Role of Joule heating on current saturation and transient behavior of graphene transistors *IEEE Electron. Device Lett.* **34** 166–8

[20] Bae M, Li Z, Aksamija Z, Martin P N, Xiong F, Ong Z, Knezevic I and Pop E 2013 Ballistic to diffusive crossover of heat flow in graphene ribbons *Nat. Commun.* **4** 1734

[21] Jang W, Chen Z, Bao W, Lau C N and Dames C 2010 Thickness-dependent thermal conductivity of encased graphene and ultrathin graphite *Nano Lett.* **10** 3909–13

[22] Li Z, Bae M-H and Pop E 2014 Substrate-supported thermometry platform for nanomaterials like graphene, nanotubes, and nanowires *Appl. Phys. Lett.* **105** 023107

[23] Asheghi M, Kurabayashi K, Kasnavi R and Goodson K E 2002 Thermal conduction in doped single-crystal silicon films *J. Appl. Phys.* **91** 5079–88

[24] Chen Z, Jang W, Bao W, Lau C N and Dames C 2009 Thermal contact resistance between graphene and silicon dioxide *Appl. Phys. Lett.* **95** 161910

[25] Koh Y K, Bae M-H, Cahill D G and Pop E 2010 Heat conduction across monolayer and few-layer graphenes *Nano Lett.* **10** 4363–8

[26] Cahill D G 1990 Thermal conductivity measurement from 30 to 750 K: the 3ω method *Rev. Sci. Instrum.* **61** 802–8

[27] Yamane T, Nagai N, Katayama S and Todoki M 2002 Measurement of thermal conductivity of silicon dioxide thin films using a 3ω method *J. Appl. Phys.* **91** 9772

[28] Seol J H *et al* 2010 Two-dimensional phonon transport in supported graphene *Science* **328** 213–6

[29] Sadeghi M M, Jo I and Shi L 2013 Phonon-interface scattering in multilayer graphene on an amorphous support *Proc. Natl Acad. Sci.* **110** 16321–6

[30] Jund P and Jullien R 1999 Molecular-dynamics calculation of the thermal conductivity of vitreous silica *Phys. Rev.* B **59** 13707–11

[31] Chen J, Zhang G and Li B 2010 Molecular dynamics simulations of heat conduction in nanostructures: effect of heat bath *J. Phys. Soc. Japan* **79** 074604

[32] Duchemin I and Donadio D 2011 Atomistic calculation of the thermal conductance of large scale bulk-nanowire junctions *Phys. Rev.* B **84** 115423

[33] Young D A and Maris H J 1989 Lattice-dynamical calculation of the Kapitza resistance between fcc lattices *Phys. Rev.* B **40** 3685–93

[34] Duchemin I and Donadio D 2012 Atomistic simulations of heat transport in real-scale silicon nanowire devices *Appl. Phys. Lett.* **100** 223107

[35] Imry Y and Landauer R 1999 Conductance viewed as transmission *Rev. Mod. Phys.* **71** S306–12

[36] Saito K, Nakamura J and Natori A 2007 Ballistic thermal conductance of a graphene sheet *Phys. Rev.* B **76** 115409

[37] Ong Z-Y, Qiu B, Xu S, Ruan X and Pop E 2018 Flexural resonance mechanism of thermal transport across graphene–SiO_2 interfaces *J. Appl. Phys.* **123** 115107

[38] Plimpton S 1995 Fast parallel algorithms for short-range molecular dynamics *J. Comput. Phys.* **117** 1–19

[39] Lindsay L and Broido D A 2010 Optimized Tersoff and Brenner empirical potential parameters for lattice dynamics and phonon thermal transport in carbon nanotubes and graphene *Phys. Rev.* B **81** 205441

[40] Robertson M J, Tirado-Rives J and Jorgensen W L 2015 Improved peptide and protein torsional energetics with the OPLS-AA force field *J. Chem. Theory Comput.* **11** 3499–509

[41] Bussi G, Donadio D and Parrinello M 2007 Canonical sampling through velocity rescaling *J. Chem. Phys.* **126** 014101

[42] van Beest B W H, Kramer G J and van Santen R A 1990 Force fields for silicas and aluminophosphates based on *ab initio* calculations *Phys. Rev. Lett.* **64** 1955–8

Supplementary Information:

Thermal Transport Across Graphene Step Junctions

Miguel Muñoz Rojo[1,2, †], Zuanyi Li[1,†], Charles Sievers[3], Alex C. Bornstein[1], Eilam Yalon[1], Sanchit Deshmukh[1], Sam Vaziri[1], Myung-Ho Bae[4], Feng Xiong[5], Davide Donadio[3, *] and Eric Pop[1,6,7,*]

[1]*Department of Electrical Engineering, Stanford University, Stanford, CA 94305, USA*

[2]*Department of Thermal and Fluid Engineering, University of Twente, Enschede, 7522 NB, The Netherlands*

[3]*Department of Chemistry, University of California Davis, Davis, CA 95616, USA*

[4]*Korea Research Institute of Standards and Science, Daejeon 34113, Republic of Korea*

[5]*Department of Electrical & Computer Engineering, University of Pittsburgh, Pittsburgh, PA 15261, USA*

[6]*Department of Materials Science & Engineering, Stanford University, Stanford, CA 94305, USA*

[7]*Precourt Institute for Energy, Stanford University, Stanford, CA 94305, USA*

[*]*Corresponding authors e-mail: epop@stanford.edu and ddonadio@ucdavis.edu*

[†]*These authors contributed to this work equally*

Table of Contents

S1. Device fabrication for thermal characterization of graphene layer junction

Highly crystalline graphite (carbon > 99.75%) from Graphene Supermarket was mechanically exfoliated with Scotch[TM] tape onto SiO_2 (~295 nm) on Si substrate chips of ~ 1×1 cm^2 size. Then, an optical microscope was used to carry out an exhaustive search for graphene junctions with lengths larger than ~8 μm and an extension of the layers at each side of the junction of more than ~2 μm. These dimensions were required to pattern our metal lines. Figure S1a and S1b show optical pictures of these samples which correspond to 1L-2L and 2L-4L graphene junctions, respectively. The small white arrows point out the location of the junction.

Electron beam (e-beam) lithography (JEOL JBX-6300FS Electron Beam Lithography System) was used to pattern the heater and sensor lines at each side of the junction. This procedure required of three lithography steps. The first one consisted on patterning global markers which helped us to locate the flakes in a coarse way. Then, we patterned a set of smaller markers, i.e. chip markers, around the flake of interest for finer alignment. The heater and sensor lines have a width of ~200 nm and a length of ~5 μm. They must be patterned at each side of the junction with a separation of only ~400 nm. That separation is smaller than the thermal healing length and makes possible to be sensitive to temperature changes at the sensor. The chip markers are essential for achieving such fine alignment. The third step consisted of patterning the heater and sensor lines as well as the electrodes pads. The e-beam dose used for the lines was 800 μC/cm^2 and we used the e-beam automatic alignment for the global and chip markers. We used two resist layers in each lithography step, made of a first layer of PMMA 495 and a second layer of PMMA 950 that were spin coated on the samples at 4000 rpm during 40 seconds and baked at 180ºC during 10 minutes.

We used an e-beam evaporator (AJA-International) to first deposit 40 nm of SiO_2 and next, on top of it, 3 nm titanium (Ti) and 35 nm of palladium (Pd). On the one hand, the SiO_2 provides electrical insulation between the metal but thermal contact with the graphene underneath. On the other hand, palladium was chosen as the thermo-resistive element since it is one of the metals with higher temperature coefficient of resistance (TCR). Figure S1c and S1d show scanning electron microscopy (SEM) images of the 1L-2L and 2L-4L junction samples after metal evaporation and lift off, respectively. The scanning electron images show that the metal lines are located on either side of the junctions. All SEM images were taken after all measurements were completed.

**a**

c

b

d
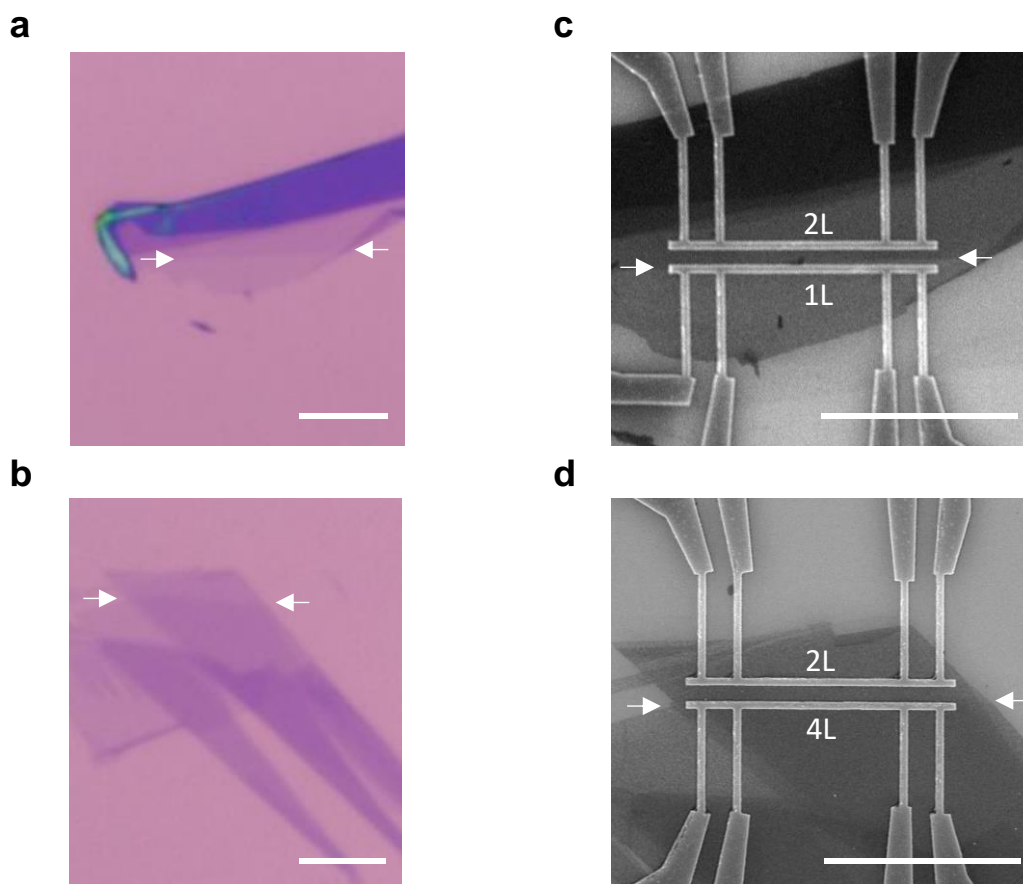
Figure S1 | Device fabrication. a) and b) show optical images of the graphene flakes with 1L-2L and 2L-4L junctions respectively. c) and d) show SEM images of the same flakes after fabricating the metal lines at the junction. The arrows point out where the graphene junctions are located.

S2. Raman spectroscopy

The number of graphene layers was characterized by Raman spectroscopy as follows. Raman spectroscopy was carried out using a Horiba LabRam instrument with a 532 nm laser and 100 × objective with N.A. = 0.9. The area of the junctions was scanned with a step size of 150 nm and applied laser power of 160 µW. The laser spot diameter obtained by the knife-edge method was < 400 nm. We analyzed the spectra of several representative locations on both sides of the junctions by removing the baseline and fitting the 2D (G') peak [1] with different number of Lorentzians. The number of layers was determined following references [2–5] by inspecting: i) the number of Lorentzians that best fit the 2D peak [2], ii) the ratio of the 2D/G peak area [3], iii) the G-band frequency [3–5] and iv) 2D peak position and width [3,5].

The peak fitting with Lorentzians of a representative location for devices 1 (1L-2L) and 2 (2L-4L) are shown in Figure S2c and Figure S2e, respectively. Figure S2 and S3 show an optical image and maps of the 2D peak area, 2D/G area ratio, 2D/G peak ratio, and 2D and G bands peak positions obtained by fitting a *single* Lorentzian to the full Raman map of devices 1 (1L-2L) and 2 (2L-4L), respectively. Note that the number of layers was identified by attempting to fit different

number of Lorentzians (only the 1L is best fitted with a single Lorentzian) [2], but the map shows the fitted results of a single Lorentzian in order to map a single measured peak position, single peak height *etc.* for each pixel.
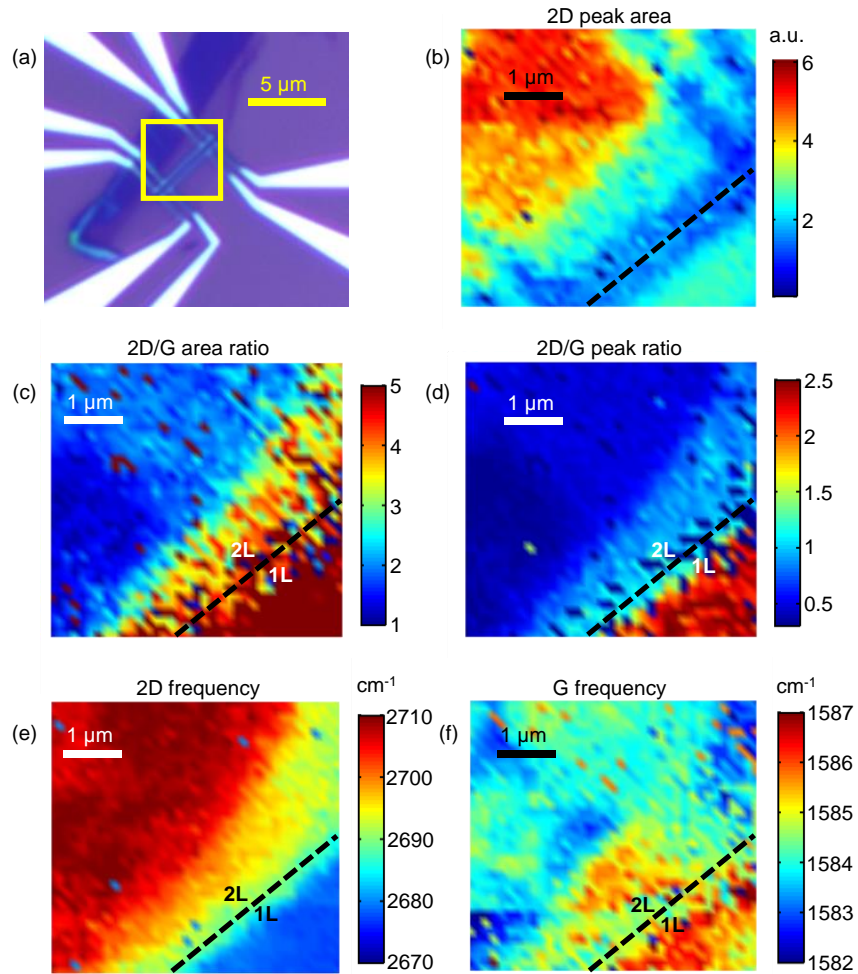

Figure S2 | Raman maps of device 1 (1L-2L). (a) Optical image of the junction. Raman maps of (b) integrated area under the 2D peak, (c) 2D/G area ratio, (d) 2D/G peak intensity ratio, (e) 2D peak position, and (f) G peak position. The dashed line indicates the junction location.
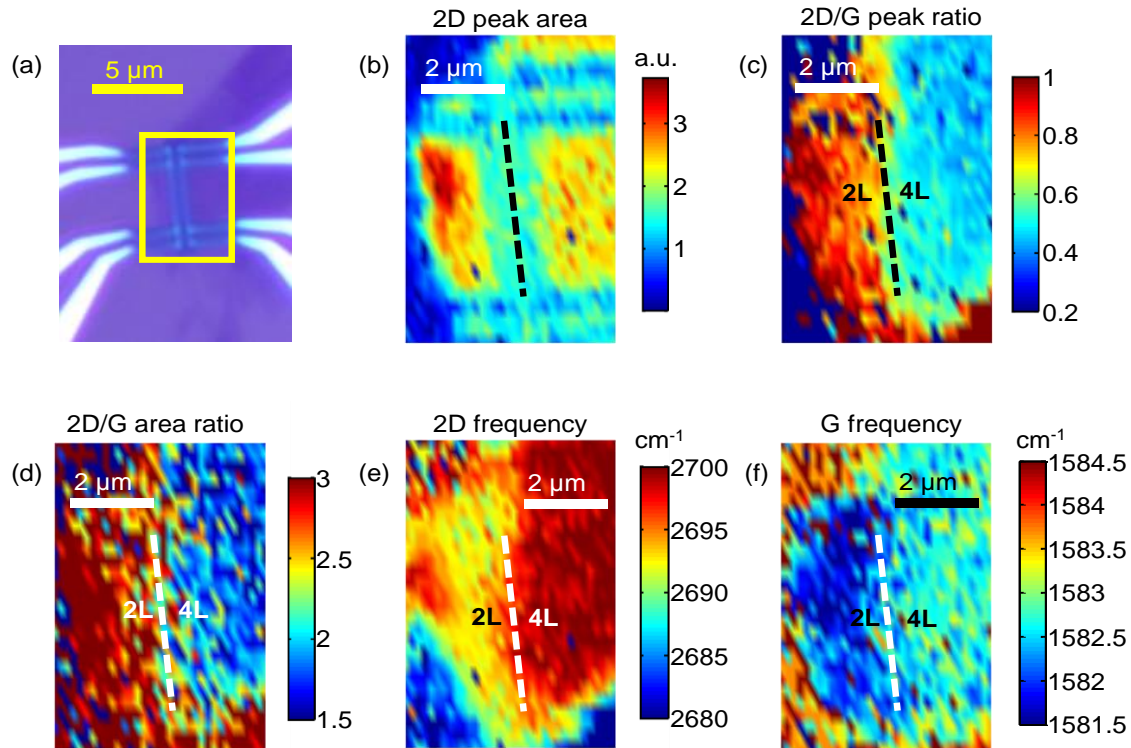
Figure S3 | Raman maps of device 2 (2L-4L). (a) Optical image of the junction. Raman maps of (b) integrated area under the 2D peak, (c) 2D/G area ratio, (d) 2D/G peak intensity ratio, (e) 2D peak position, and (f) G peak position. The dashed line indicates the junction location.

S3. Ellipsometry: Silicon oxide thickness measurements

We used a Woollam M2000 spectroscopic ellipsometer to extract thickness of SiO_2 films used. The tool uses a Xe Arc Lamp as the light source and measures reflected light from the sample surface across the 210 – 1600 nm spectrum. We used data from three angles of incidence 65°, 70° and 75° to extract thickness. At each angle, we fitted the model for optical constants of thermal SiO_2 on bulk Si to the change in polarization of the reflected light from the sample surface. The fit for the model let us extract the thickness and optical constant of the SiO_2 film. Figure S4 shows the fit of our model to the polarized light phase change data versus wavelength of incident light for the SiO_2 substrates used in our devices. The extracted thickness is 294.4 nm for the graphene junction samples and 295.5 nm for the control sample. These measurements showed sub-Å fitting error. The thickness of the silicon underneath was 500 μm. We etched the SiO_2 of the surface of the substrate using hydrofluoric acid in order to measure its electrical conductivity, which was determined to be 0.0038 Ω·cm (sheet resistivity probe analyzer I280-Desktop four-point probe, Four Dimensions Inc.). These parameters are essential for the finite element modeling simulations as well as the dimensions of the heater and sensor lines which were measured using SEM.
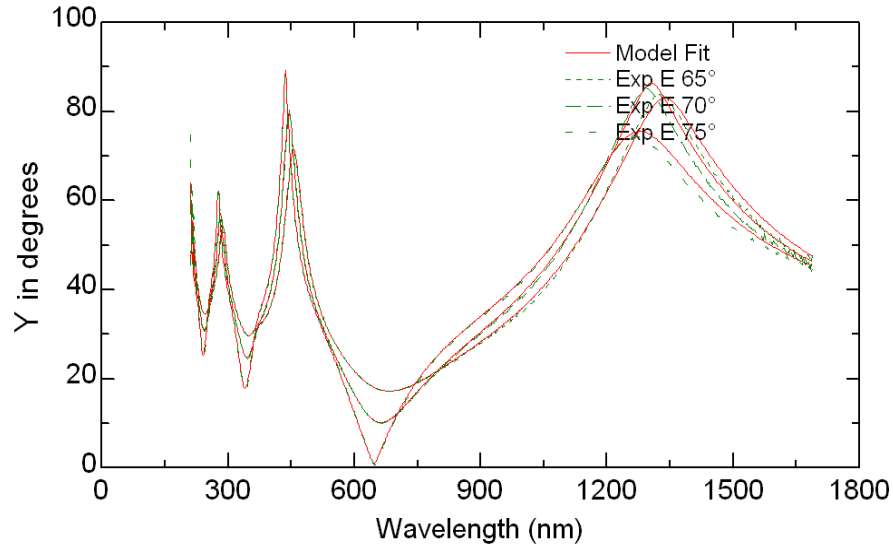
Figure S4 | Ellipsometry. Fit of our model to the polarized light phase change data versus wavelength of incident light for the SiO_2 substrates used in our devices.
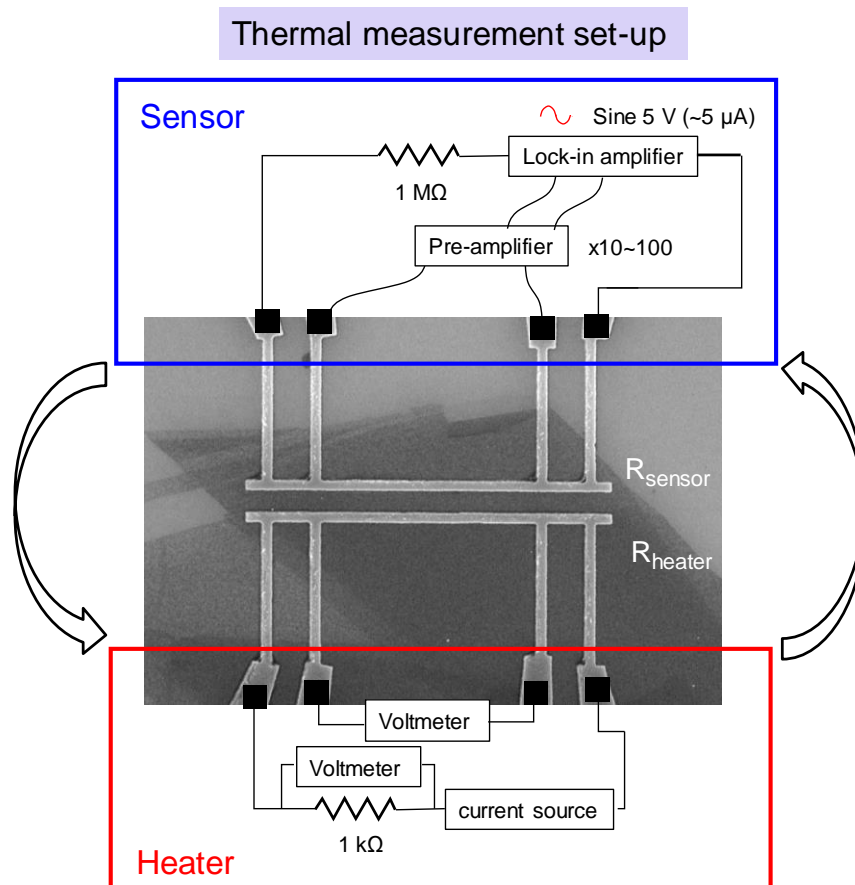
S4. Experimental set-up

Figure S1c and S1d show that the metal lines have four electrical probe connections, two for applying current and another two for measuring voltage across the line. These probes end in electrical pads of 300×300 μm^2 to enable wire bonding. A wedge wire bonder (West Bond 7476E Wedge-Wedge Wire Bonder) was used for that purpose. However, we noticed that the metal lines that we fabricated were broken during the wire bonding of the device. We believe that this was caused by the sonication that is produced during the bonding, which propagates a vibration to the small metal lines breaking them, as well as to the presence of possible electrical spikes. We avoided this damage by patterning external electrical pads separated ~ 100 μm from the inner device pads. These external pads were used for wire bonding avoiding any damage that could be produced during this step. Then, we electrically connected the inner device pads with the external ones using conductive silver-filled epoxy (World Precision Instruments). For that purpose, we used a micro-probe and manually put a drop in the gap between electrical pads. Figure S5a shows an optical image of the two devices that were measured after wire bonding and with silver epoxy drops connecting the pads. Figure S5b shows an optical image zoom in the two devices measured, 1L-2L and 2L-4L graphene junction samples. Finally, the chip carrier where the sample was mounted and wire-bonded was loaded in the cryostat. The sample was glued onto the chip carrier using silver paste. In addition to the thermocouple at the base of the chip carrier, another thermocouple was located on the surface of the chip carrier to measure the temperature and compare it to the one at the base of the chip. Figure S5c shows a picture of the chip carrier loaded in the arm of the cryostat, where the sample and the thermocouple can be seen.
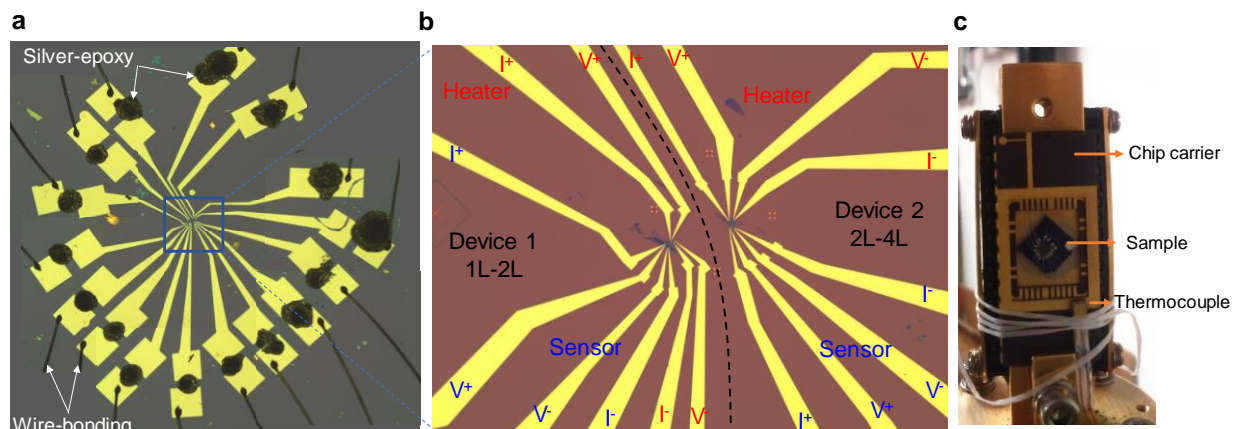
Figure S5 | Optical images of samples. a) Optical image of the full devices. This image shows the external pads that were used for wire bonding and the silver conductive epoxy drops that connects them electrically with the inner pads of the device. b) Optical image zoom in the 1L-2L and 2L-4L devices and a schematic map of the electrical connections of the four-probe electrodes for both the heater and sensor. c) Picture of chip carrier loaded in the arm of the cryostat. The sample is glued onto the chip carrier using silver paint and a thermocouple is attached to the surface of the chip to measure the temperature at the surface.

The experimental set up is illustrated in Figure S6. A DC current source (Keithley DC/AC source 6220) was used to apply current (<1 mA) to the heater metal line. The current provided by the source was also measured experimentally using a 1 kΩ resistor and a voltmeter (Keithley Multimeter 2000). The voltage between the middle probes of the lines was measured using another voltmeter (Keithley Multimeter 2000). The line heating was varied by sweeping the current, i.e. Joule heating. The changes in the electrical resistance of the sensor were measured using a lock-in amplifier (Stanford Research Systems SR-850). The sensor line is connected in series with 1 MΩ and a lock-in voltage of 5 V (~5 µA) is used to sense. The voltage from the voltage probes of the sensor line is amplified using a low noise pre-amplifier (Stanford Research Systems SR-560). This set up allowed us to measure accurately small changes in resistance as a consequence of temperature variations.

Figure S6 | Experimental measurement set-up. Thermal measurement set-up. A DC current source is used to apply current to the heater line. The current provided by the source was also measured experimentally using a 1 kΩ resistor and a voltmeter. The voltage between the middle probes of the lines was measured using another voltmeter. The sensor line is connected in series with 1 MΩ and a lock-in voltage of 5 V (~5 μA) is used to sense. The voltage from the voltage probes of the sensor line is amplified using a low noise pre-amplifier. The heater and sensor lines can be swapped to account for asymmetric heat flow across graphene junction, i.e. thermal rectification.

S5. Control sample: Thermal measurements of SiO_2/Si substrate

A SiO_2/Si substrate (Graphene supermarket) of ~1 × 1 cm², identical to the ones used to exfoliate graphene, was used as a control sample. The thickness of the oxide was 295.5 nm, which was measured by ellipsometry (section S3). Two four-probe metal lines, ~200 nm wide and ~ 15 μm long, were fabricated on top of the SiO_2 separated by ~400 nm. One of the lines was used as a heater while the other one was used as a sensor. The metal lines were made of 3 nm Ti and 35 nm Pd. Figure S7a and b show an optical and a SEM image, respectively, of the control sample with the metal lines on top.

a

b

Control sample
295 nm SiO$_2$
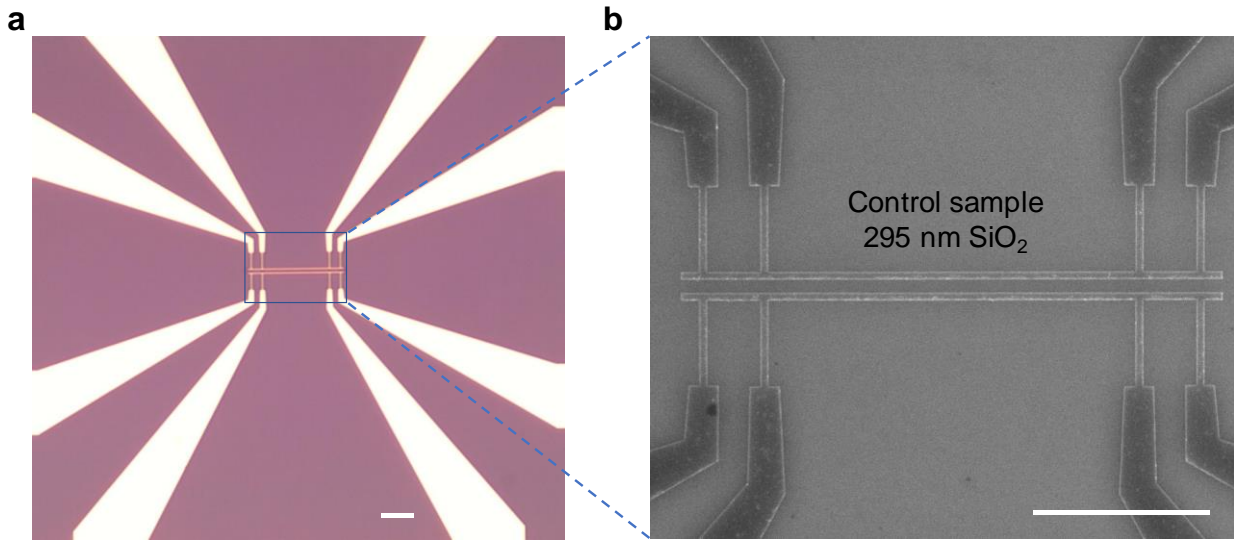
Figure S7 | Control sample. a) Optical image of the control sample on SiO$_2$ (on Si) with four probe electrodes at each metal line. b) Scanning electron microscopy image of the metal lines. Scale bars were set at 5 μm size.

Figure S8a shows a schematic drawing of the control sample with the heater and sensor on top of SiO$_2$. The metal lines were labeled to identify the current and the voltage probes for each metal line. For the temperature coefficient of resistance measurements, changes of the electrical resistance as a function of temperature were measured. For that purpose, low currents (~50 μA) were applied to the metal lines to avoid self-heating. However, this current was high enough to reduce the electrical noise and measure the resistance with high accuracy. Figure S8b shows the resistance changes of the heater and sensor lines with temperature, while Figure S8c plots *dR/dT* derived from this figure. From these data, changes in the electrical resistance of the metal lines can be correlated with temperature changes.

Figure S8d and Figure S8e show temperature variations for the heater, ΔT_H, and sensor, ΔT_S, respectively, when sweeping the power of the heater line at different temperatures. Figure S8f plots these temperature variations per heater power versus temperature. The values of the temperature dependent thermal conductivity of the SiO$_2$ on top of this Si substrate are equivalent to those publish by Bae *et al*. [6] and Cahill [7].
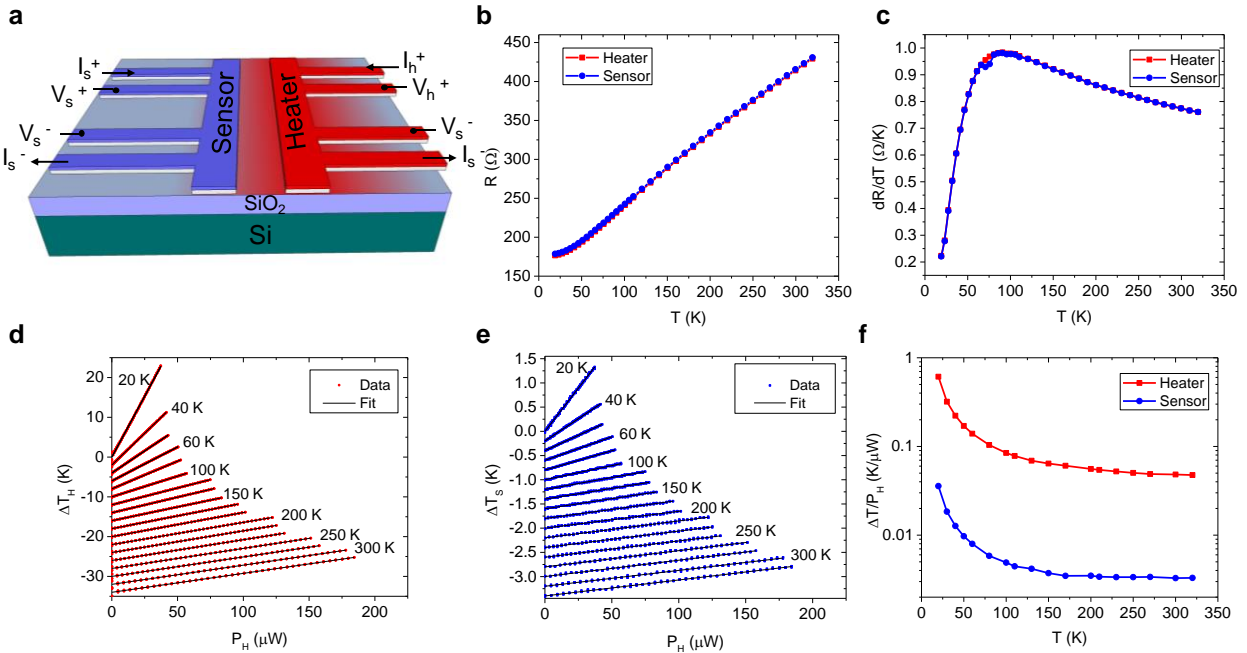
Figure S8 | Control sample. a) Schematic drawing of the heater and sensor line on top of the Si/SiO$_2$ control sample. The current, I, and voltage, V, probes are labeled in the image. b) and c) show the resistance, R, and dR/dT versus temperature for the heater (red symbols) and the sensor (blue symbols), respectively. d) and e) shows the temperature variation of the heater, ΔT_H, and sensor, ΔT_S, when sweeping the heater power for different temperatures, respectively. f) Temperature variations per heater power, $\Delta T/P_H$, as a function of temperature for the heater and the sensor.
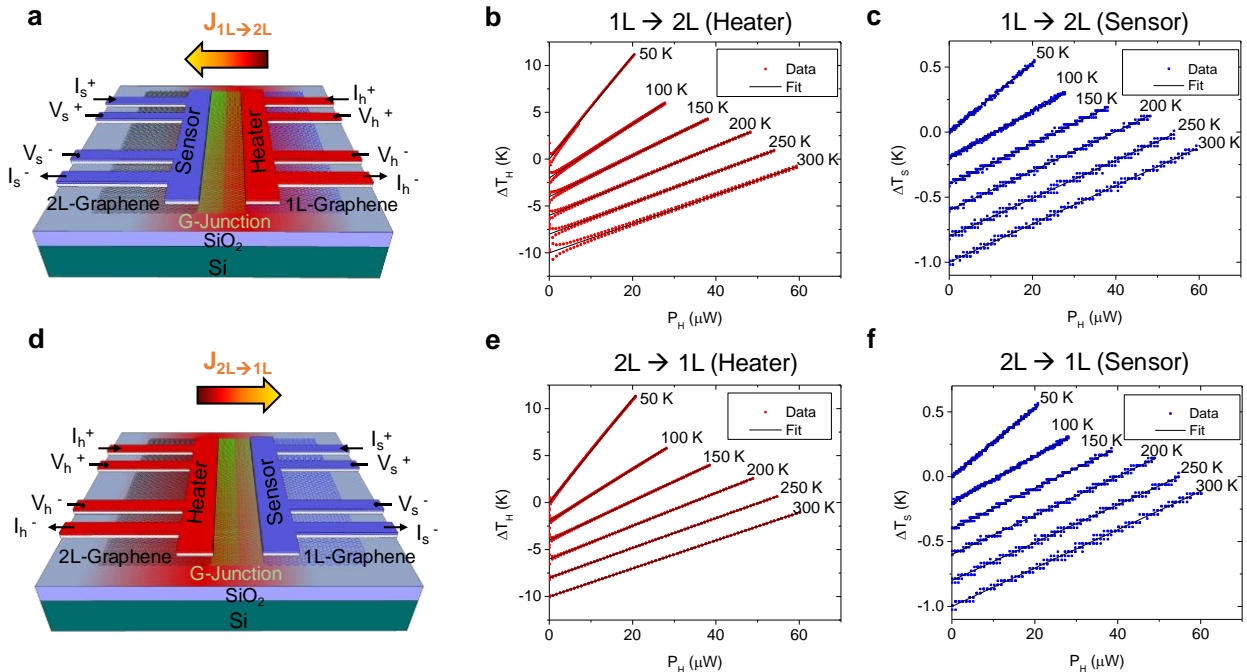
S6. 1L-2L graphene junction: Thermal measurements

The temperature coefficient of resistance of the heater and sensor lines for the 1L-2L graphene junction sample was determined experimentally using the same measuring conditions and procedure as it was shown for the control sample in section S5. However, for the graphene junction samples, we studied the heat flow in two different configurations in order to account for possible rectification effects, i.e. when heat flows from 1L to 2L of graphene as well as from 2L to 1L. For that purpose, the heater and sensor were swapped. Figure S9 shows the calibration for heater and sensor in these two configurations. The results show excellent agreement in the values of the resistance as a function of temperature for the metal lines in the two different configurations. From these plots, changes in the electrical resistance of the metal lines could be then correlated with temperature changes.
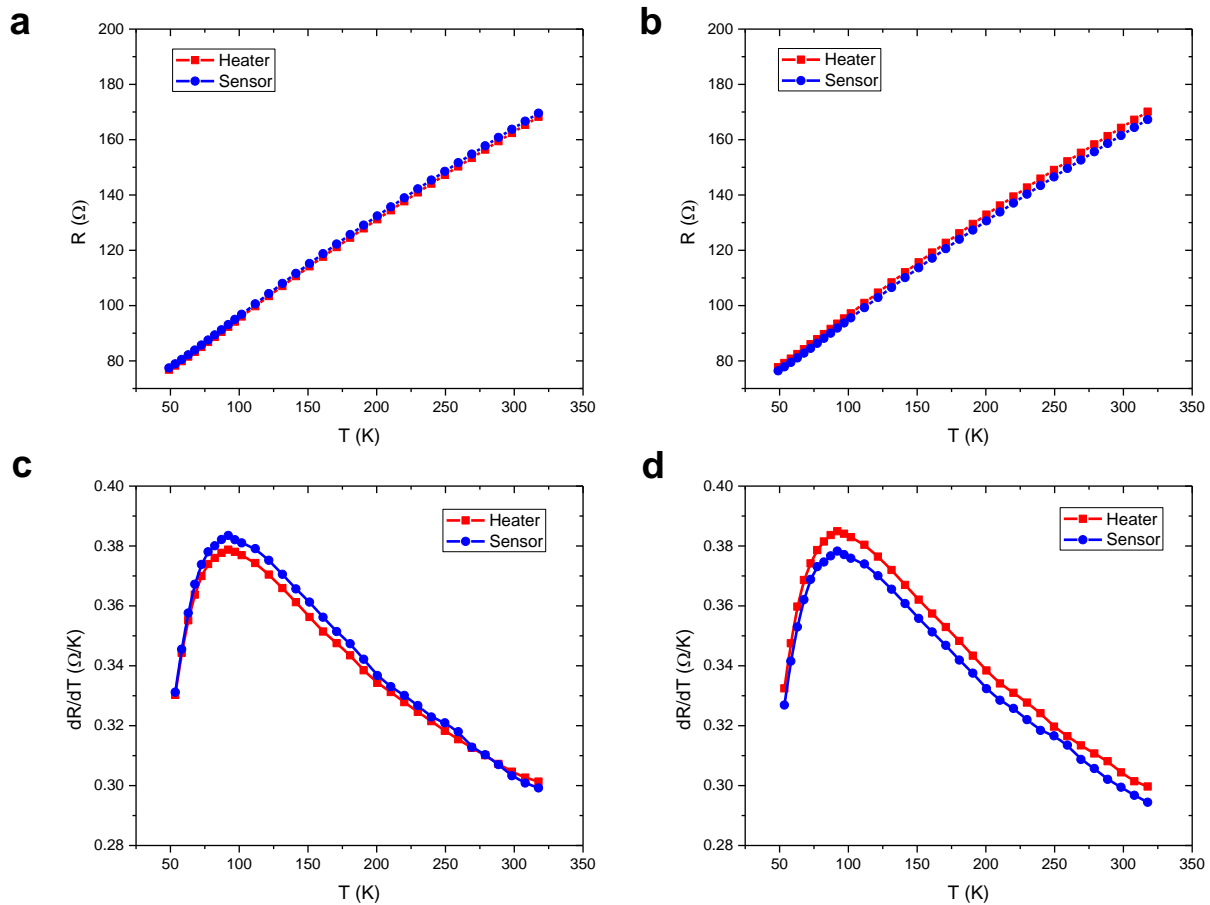
Figure S9 | Thermal measurements 1L-2L device. a) and b) show the electrical resistance of the heater and sensor lines as a function of temperature for the two different measuring configurations, i.e. before and after being swapped. c) and d) show *dR/dT* versus temperature for the heater (red symbols) and the sensor (blue symbols) obtained from a) and b), respectively.

For thermal measurements, the current applied to the heater line was swept and the changes of temperature at the heater and sensor recorded. On the one hand, Figure S10a shows schematically the first configuration, where the heater was located in 1L graphene and the sensor in 2L graphene, i.e. the heat flows from 1L to 2L. The temperature variations for the heater, ΔT_H, and sensor, ΔT_S, when sweeping the power of the heater line at different temperatures are plotted in Figure S10b and c, respectively. On the other hand, Figure S10d illustrates the second configuration, where the heater was positioned in 2L graphene and the sensor in 1L graphene, i.e. the heater and sensor are swapped and the heat flows now from 2L to 1L graphene. Figure S10e and f show ΔT_H and ΔT_S vs heater power in this second configuration. It is worth noting that there is no way to calculate the heat power going through graphene only, even with finite element modeling (FET), because heat continuously sinks into the substrate as it goes through graphene. Although the finite element model gives an accurate value of the overall thermal conductance, the conductance right at junction cannot be separated. The error bars of the thermal conductivity obtained with FET was calculated using the classical partial derivative method.

Figure S10 | Thermal measurements 1L-2L device. a) Schematic drawing for the first measuring configuration, where the heat flows from 1L to 2L graphene. b) and c) show the temperature variation of the heater, ΔT_H, and sensor, ΔT_S, when sweeping the heater power for different temperatures, respectively. d) Schematic drawing for the second measuring configuration, where the heater and sensor are swapped and the heat flows now from 2L to 1L graphene. e) and f) shows ΔT_H and ΔT_S, vs heater power for different temperatures in this configuration, respectively.
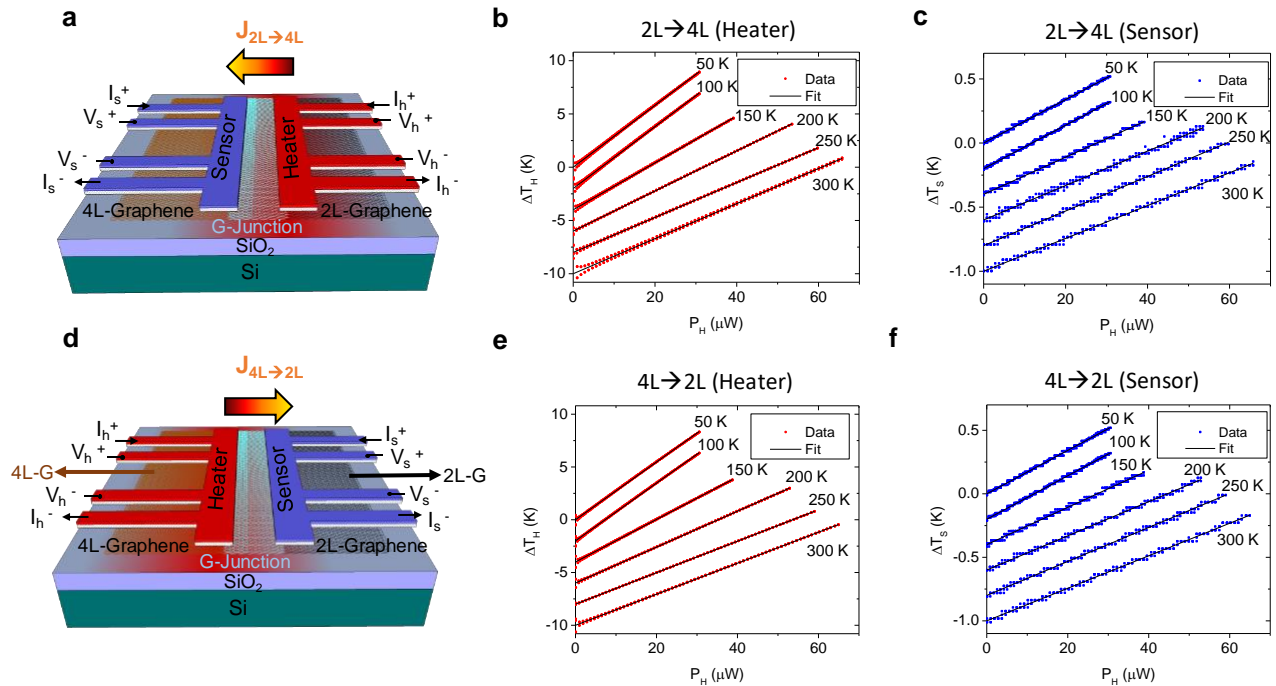
S7. 2L-4L graphene junction: Thermal measurements

Thermal measurements of 2L-4L graphene junction sample were carried out in the same was as it was explained in section S6 for the 1L-2L graphene junction sample. Figure S11 shows the calibration for heater and sensor in the two configurations, before and after the heater and sensor are swapped. As for the 1L-2L device, the results show excellent agreement in the values of the resistance as a function of temperature for the metal lines in the two different configurations.

a

b

c

d
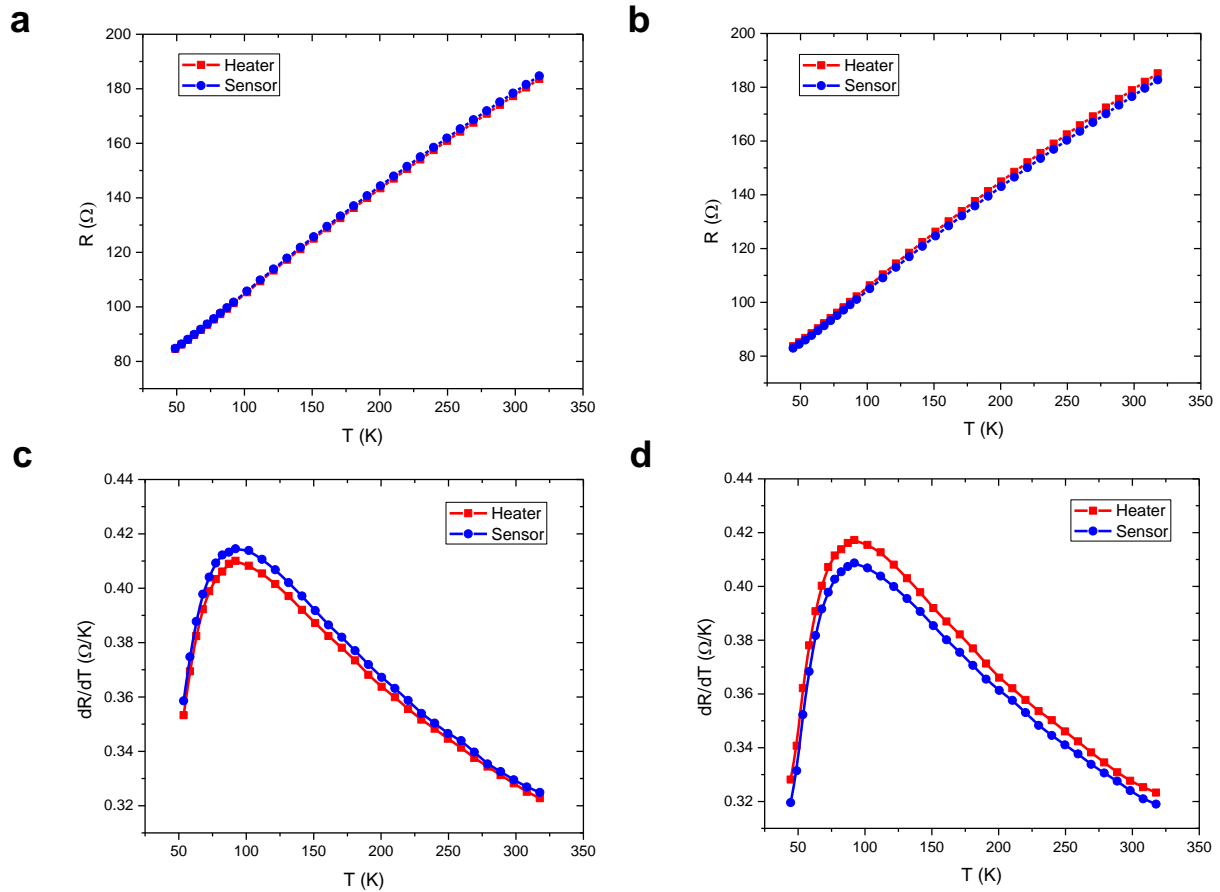
Figure S11 | Thermal measurements 2L-4L device. a) and b) show the electrical resistance of the heater and sensor lines as a function of temperature for the two different measuring configurations, i.e. before and after being swapped. c) and d) show *dR/dT* versus temperature for the heater (red symbols) and the sensor (blue symbols) obtained from a) and b), respectively.

Then, thermal measurements were carried out in the same way as for the 1L-2L graphene junction device. The heat flow was also studied in both directions to account for possible rectification effects using two measuring configuration, i.e. swapping the heater and sensor. Figure S12 a shows schematically the first configuration, where the heater was located in 2L graphene and the sensor in 4L graphene, i.e. the heat flows from 2L to 4L. The temperature variations for the heater, ΔT_H, and sensor, ΔT_S, when sweeping the power of the heater line at different temperatures are plotted in Figure S12b and c, respectively. On the other hand, Figure S12d illustrates the second configuration, where the heater was positioned in 4L graphene and the sensor in 2L graphene, i.e. the heater and sensor are swapped and the heat flows now from 4L to 2L graphene. Figure S12e and f show ΔT_H and ΔT_S vs heater power in this second configuration.

Figure S12 | Thermal measurements 2L-4L device. a) Schematic drawing for the first measuring configuration, where the heat flows from 2L to 4L graphene. b) and c) show the temperature variation of the heater, ΔT_H, and sensor, ΔT_S, when sweeping the heater power for different temperatures, respectively. d) Schematic drawing for the second measuring configuration, where the heater and sensor are swapped and the heat flows now from 4L to 2L graphene. e) and f) shows ΔT_H and ΔT_S, vs heater power for different temperatures in this configuration, respectively.

S8. Molecular dynamics (MD) simulations

We ran NEMD simulations on a multilayer graphene junction to determine the thermal conductance. The conductance is inversely proportional to temperature differential and proportional to heat flux based on Fourier's law. Therefore, smaller temperature differential and larger flux will yield larger conductance. Figure S13 shows both the flux and the temperature profile for temperature perturbations applied to a 50 nm long suspended multilayer graphene device, where the multilayer runs for half the device. Both forward and reverse heat fluxes are simulated through a reversal of a temperature perturbation using Langevin baths as described in the main text. The flux is a running average of the steady state heat flux. Figure S14 shows a set of NEMD plots similar to Figure S13 but at larger thermostating conditions which also proves that thermal rectification remains unlikely even at large temperature differences.
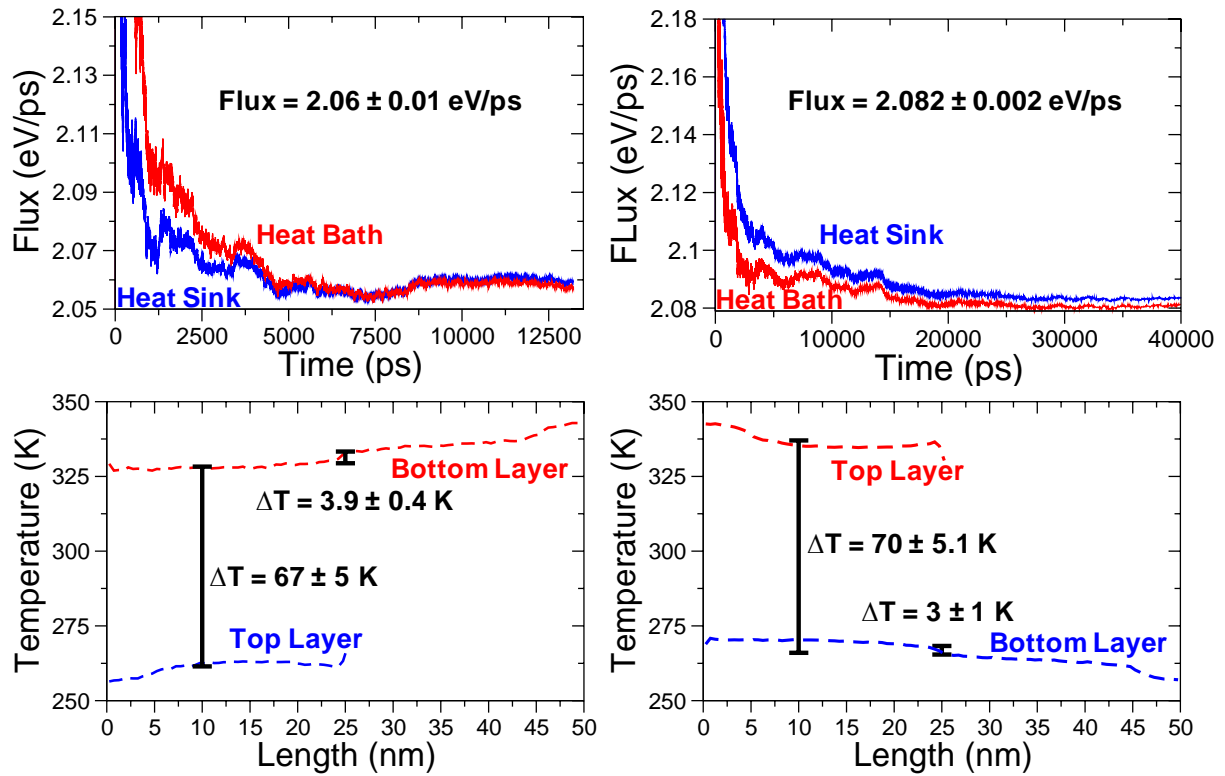
Figure S13: Heat flux in the direction from the bottom layer to top layer (top left plot). Heat flux in the direction from top layer to bottom layer (top right plot). Temperature profile of multilayer graphene junction with heat flux in the direction from bottom layer to top layer (bottom left plot). Temperature profile of multilayer graphene junction with heat flux in the direction from top layer to bottom layer (bottom right). The relaxation time was set to 1 ps for this trial.
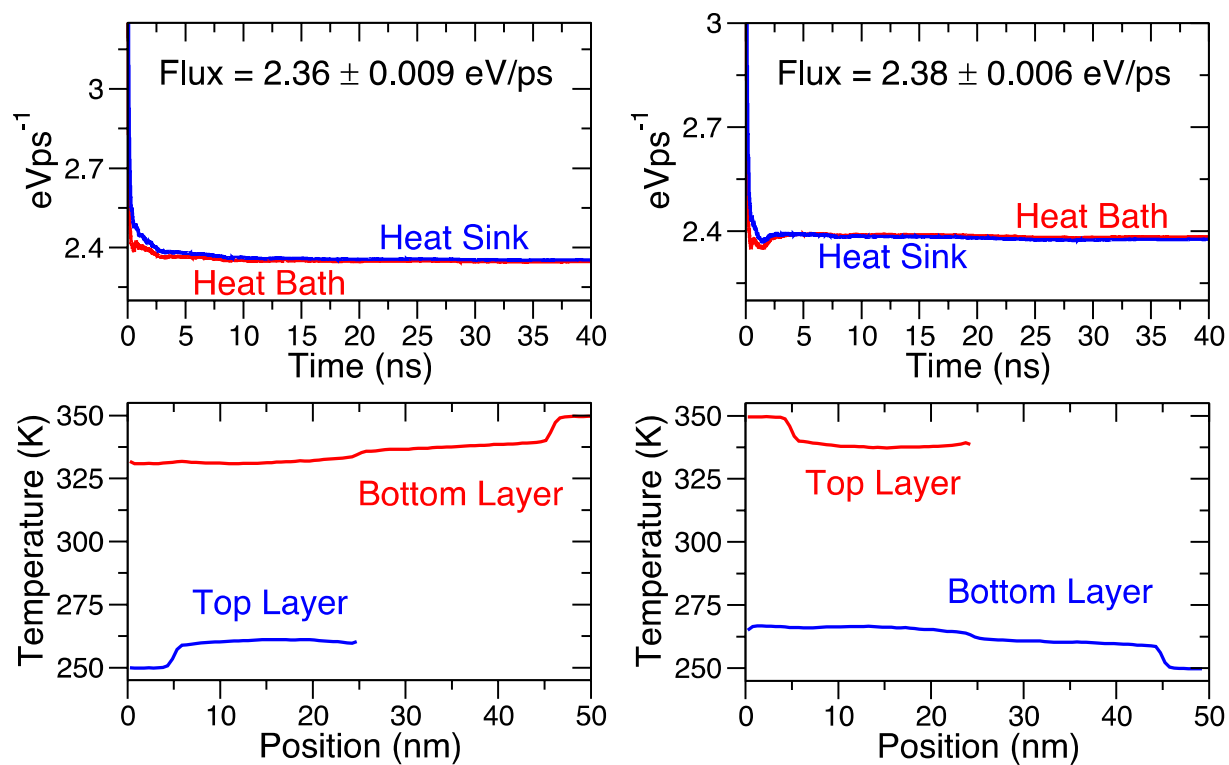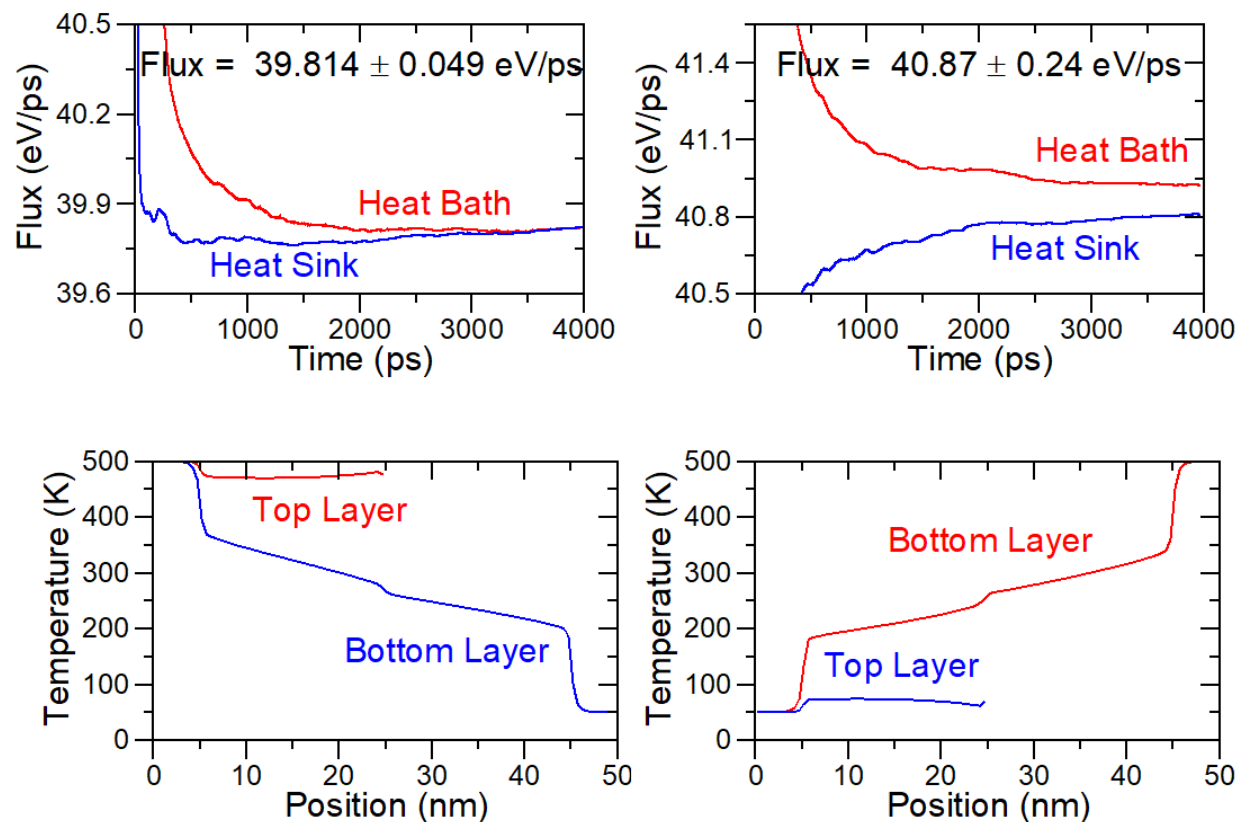
Figure S14. Similar set of plots as in Figure S13 but in this case the thermostat relaxation time is set to 0.05 ps. The change in thermostat relaxation time ensures that the bath temperatures are reached, however artificial thermal resistance builds up at the edges of the thermostatted region. Negligible thermal rectification is observed.
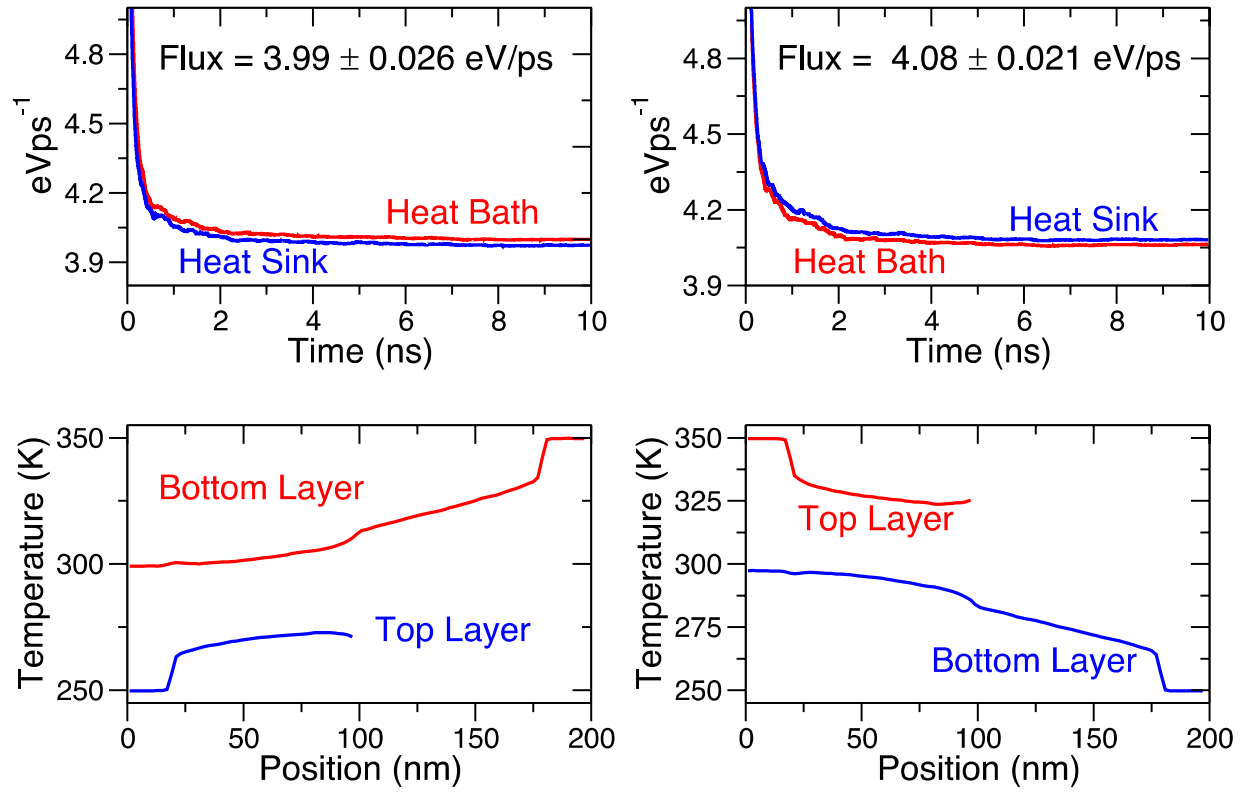
Figure S15. Similar set of plots as in Figure S14 but in this case the device length is 200 nm. The length is on the same size order as the experiment. Negligible thermal rectification is observed.

Figure S16. Similar set of plots as in Figure S13 but in this case both layers are thermostated with a temperature gradient that goes from 50K to 500K. In this case, both layers are thermostated in the bilayer portion. Similar NEMD plots where obtained when only the top layer is thermostated in the bilayer region. Negligible thermal rectification is observed.

S9. Lattice dynamics calculations

Figure S17 was produced by lattice dynamics calculations as described in the main text. The leftmost plot in Figure S17 shows a trend of the increase in optical mode transmission with increase in overlap length. There is no trend between overlap length and the major heat carrying acoustic modes. The two plots on the right side of Figure S17 are both transmission functions decomposed by mode polarization. The top right plot in Figure S17 is supported on quartz, same as the plot on the left. The bottom right plot is suspended and has a larger transmission than the supported case, which is to be expected because the substrate reduces the space in which flexural modes can oscillate within. The two decomposed transmission function plots clearly show that the transmission of flexural modes dominate, therefore, heat transport is almost exclusively carried through out of plane modes.
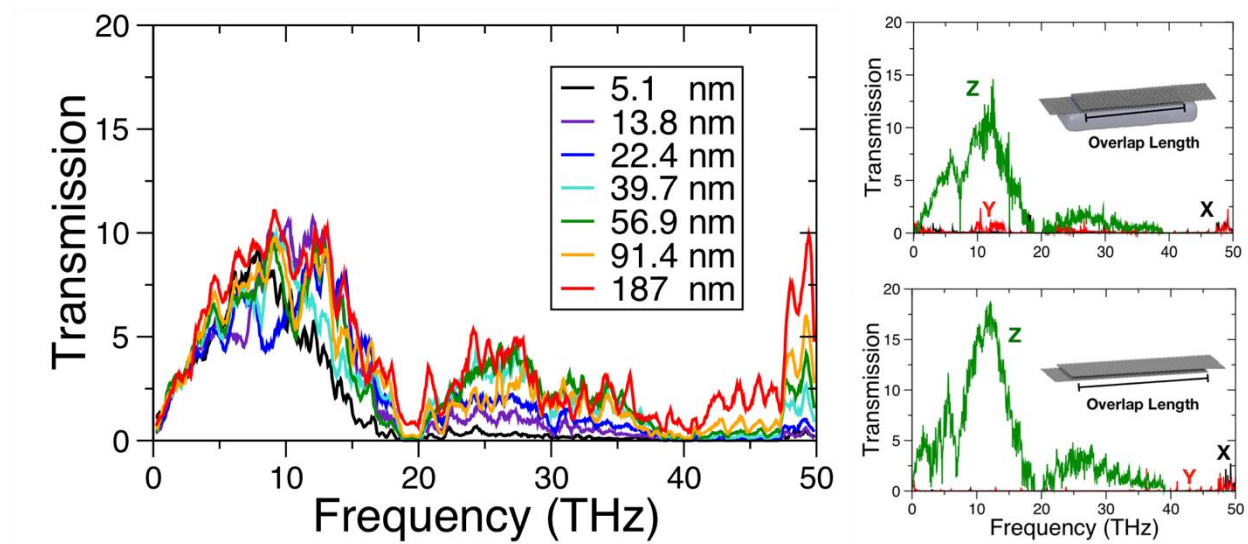
Figure S17: Transmission functions for different overlap lengths overlaid one another (left). Polarization decomposed transmission function of supported multilayer graphene junction (top right). Polarization decomposed transmission function of suspended multilayer graphene junction (bottom right).

S10.　3D Finite element simulations and uncertainty analysis

We use COMSOL software to extract the thermal properties of our graphene junction and control samples. To do so we set up a three-dimensional (3D) finite element model (FEM) to simulate the experimental structures and fit to our thermal measurements (see Figure 1f as an example). The simulations were performed by following the method described in our previous work.[6] [8]To extract the thermal conductivities shown in Figures 3c and 3d, they are varied as fitting parameters until $\Delta T_S/P_H$ and $\Delta T_H/P_H$ from FEM match with those from experiments (Expt.). Take the 1L-2L sample as an example, k_1, k_2, $k_{1\text{-}2}$, and $k_{2\text{-}1}$ are fitted until the following equations are satisfied simultaneously,

$$\Delta T_S(k_1, k_{1-2}, k_2)/P_H\big|_{\text{FEM}} = \Delta T_S/P_H\big|_{\text{Expt}} \qquad (1\text{L}\rightarrow 2\text{L}),$$

$$\Delta T_H(k_1, k_{1-2}, k_2)/P_H\big|_{\text{FEM}} = \Delta T_H/P_H\big|_{\text{Expt}} \qquad (1\text{L}\rightarrow 2\text{L}),$$

$$\Delta T_S(k_2, k_{2-1}, k_1)/P_H\big|_{\text{FEM}} = \Delta T_S/P_H\big|_{\text{Expt}} \qquad (2\text{L}\rightarrow 1\text{L}),$$

$$\Delta T_H(k_2, k_{2-1}, k_1)/P_H\big|_{\text{FEM}} = \Delta T_H/P_H\big|_{\text{Expt}} \qquad (2\text{L}\rightarrow 1\text{L}).$$

We used a single laptop computer to implement the fitting process by using MATLAB to interface directly with COMSOL. It takes several hours to reach a best-fit of (k_1, k_2, $k_{1\text{-}2}$, $k_{2\text{-}1}$) at each measured ambient temperature point.

The uncertainty of extracted thermal conductivity k can be estimated by the classical partial derivative method:

$$\frac{U_k}{k} = \sqrt{\sum_i \left(S_i \times \frac{U_{x_i}}{x_i} \right)^2} \; ,$$

where U_k is the total uncertainty in the extracted thermal conductivity k, U_{xi} is the uncertainty of the i-th independent input parameter x_i, and the dimensionless sensitivity S_i is defined by

$$S_i = \frac{x_i}{k} \frac{\partial k}{\partial x_i} \; .$$

The partial derivative in S_i is evaluated numerically by giving small perturbation of each parameter x_i around its typical value and redoing the extraction simulation to obtain the change of k. The estimated uncertainties are plotted as error bars in Figures 3c, 3d, 3e, and 3f, where uncertainties of the junction thermal conductivity are ~10%−20%, and those for non-junction parts are ~30%−40%.

Supporting References:

[1]   Ferrari A C and Basko D M 2013 Raman spectroscopy as a versatile tool for studying the properties of graphene *Nat. Nanotechnol.* **8** 235–46

[2]   Malard L M, Pimenta M A, Dresselhaus G and Dresselhaus M S 2009 Raman spectroscopy in graphene *Phys. Rep.* **473** 51–87

[3]   Graf D, Molitor F, Ensslin K, Stampfer C, Jungen A, Hierold C and Wirtz L 2007 Spatially Resolved Raman Spectroscopy of Single- and Few-Layer Graphene *Nano Lett.* **7** 238–42

[4]   Gupta A, Chen G, Joshi P, Tadigadapa S and Eklund 2006 Raman Scattering from High-Frequency Phonons in Supported n -Graphene Layer Films *Nano Lett.* **6** 2667–73

[5]   Yoon D, Moon H, Son Y-W, Choi J S, Park B H, Cha Y H, Kim Y D and Cheong H 2009 Interference effect on Raman spectrum of graphene on SiO_2/Si *Phys. Rev. B* **80** 125422

[6]   Bae M, Li Z, Aksamija Z, Martin P N, Xiong F, Ong Z, Knezevic I and Pop E 2013 Ballistic to diffusive crossover of heat flow in graphene ribbons *Nat. Commun.* **4** 1734

[7]   Cahill D G 1990 Thermal conductivity measurement from 30 to 750 K: the 3ω method *Rev. Sci. Instrum.* **61** 802–8

[8]   Li Z, Bae M-H and Pop E 2014 Substrate-supported thermometry platform for nanomaterials like graphene, nanotubes, and nanowires *Appl. Phys. Lett.* **105** 023107